



Internship Report 3A

Quantitative ultrasound imaging of roughness, application to bone health assessment

12 February 2024 - 26 July 2024

SALOMÉ VIGNAT

BIOMEDICAL ENGINEERING
MEDICAL IMAGING AND THERAPY

2023-2024

Laboratory tutor :

QUENTIN GRIMAL
quentin.grimal@sorbonne-universite.fr
AMADOU DIA
amadou.dia@sorbonne-universite.fr

University tutor :

CHARLOTTE VENDRELY
charlotte.Vendrely@grenoble-inp.fr

Laboratory coordinates :

Sorbonne Université, INSERM, CNRS,
Laboratoire d'Imagerie Biomédicale, LIB,
15 Rue de l'École de Médecine,
75006 Paris

Contents

Glossary	3
List off figures	6
List off tables	6
Introduction	7
1 Internship environment presentation	8
2 Context and Approach of the Study	9
2.1 Introduction to the medical context: Osteoporosis	9
2.2 Basics of ultrasound imaging	10
2.3 Principle of Bone Ultrasound Imaging	13
2.3.1 Bone Imaging	13
2.3.2 Specularity	15
3 Ex-Vivo Bone Parametric Study	18
3.1 X-Ray Ex-Vivo Images	18
3.2 Analysis of the endosteal interface microstructure	19
3.2.1 Image processing method	19
3.2.2 Parameters definition	21
3.2.3 Analysis of the intra-cortical micro-structure	23
4 Analysis of the endosteal interface specular response, a simulation study	25
4.1 General parameters of the simulation	25
4.2 Generation of bone micro-structure model	26
4.2.1 Generation of simple microstructures	26
4.2.2 Generation of realistic microstructures	30
4.3 Post-process of the simulation and analysis of the results	32
4.3.1 Post processing of the simulations	32
4.3.2 Analysis and interpretation of the results	33
5 Perspective	37
Conclusion	39
References	41
A Parameters of the endosteal interface roughness on ex-vivo bones	42
B Histogram of the distributions of the pore position along the depth of the bone and their diameter	43
C Gantt diagram	44
Abstract	46

Fiche résumé

47

Glossary

LIB: Laboratory of Biomedical Imaging.

CNRS: National Center for Scientific Research.

BQ: Bone Quality, the Ultrasonics and Imaging for Bone Quality Characterization team of the Laboratory of Biomedical Imaging.

INSERM: National Institute of Health and Medical Research.

Cortical Bone: The dense cylindrical layer of bone that contains the bone marrow.

Endosteum: The inner surface of the cortical bone, thus the interface between the bone and the bone marrow.

Periosteum: The outer surface of the cortical bone that interacts with surrounding soft tissues.

Osteoporosis: A disease characterized by weakened bones and an increased risk of fractures, usually due to a reduction in bone mass and density.

Ex-Vivo: Refers to studies or experiments conducted on bone outside their natural context.

BMD: Bone Mineral Density, presently the biomarker used to discriminate osteoporotic bone.

DXA: Dual Energy X-Ray absorptiometry, method used to measure the Bone Mineral Density

Micro-CT: Micro-Computed Tomography, a high-resolution imaging technique used to visualize the internal structure of small objects, using X-Ray.

B-Mode: Brightness mode, ultrasound imaging mode representing the amplitude of the signal in each pixel.

DAS: Delay-and-Sum, beamforming method to reconstruct ultrasounds images.

FDTD: Finite-Difference Time-Domain, modelization of medium.

ROI: Region of Interest, a specified part of an image selected for detailed examination or analysis.

E.ROI: Endosteal Intra-Cortical Region of Interest, one-wavelength-wide above the endosteal interface, on the ex-vivo bone images.

S.ROI: Specular Intra-Cortical Region of Interest, one-wavelength-wide around the endosteal interface, on the specular map.

Rq : Height Root Mean Square, a measure of surface roughness, represents the square root of the average of the squares of deviations from the mean surface level.

ρ_{length} : Correlation length, a measure of surface roughness, represents the distance at which the auto-correlation is equal to $1/e$.

E.Pore : Endosteal porosity, ratio of the volume of pore and the total volume in a one-wavelength-wide above the endosteal interface.

d.Pore : Mean Diameter of the Pore in a one-wavelength-wide above the endosteal interface.

Specular Index: A metric used to quantify the specular response (reflection of acoustic waves in a single direction) indicating the intensity of reflected ultrasound waves.

$\overline{\psi_{\text{lateral}}}$: Mean Specular Index along the Lateral Position in the Region of Interest of the specular map.

$\overline{\psi_{\text{S.ROI}}}$: Mean Specular Index in the Region of Interest of the specular map.

FWHM: Full Width at Half Maximum, width of a Gaussian distribution when half the maximum amplitude is reached.

List of Figures

2	Structure of both types of bone, trabecular (top) and cortical (bottom). Reproduced from Mouchet [3]	9
3	Bone degradation and transitional zone. Derived from Zebaze [5] [6]	10
4	Basic principle of synthetic aperture ultrasound imaging, from Nikolov [8]	11
5	Ray-Path from emitter i to receiver i	12
6	Ray-Path from emitter i to receiver j in homogeneous layers	13
7	Setup for the acquisition of ultrasound data	14
8	Diffuse and specular acoustic responses	15
9	Diffuse and specular acoustic responses (d) and (e) of different profiles (b) and (c). Correlation (f) and (g) of the acoustic response with the specular model (a), from Dia [14]	17
10	Bone extraction and region of interest that is going to be imaged, from Dia [14]	18
11	Ex-Vivo Bone and delimitation of the endosteal interface (red) and the E.ROI (blue)	19
12	Resolution of the specular beamformed image, with the periosteal interface (deep blue) and the endosteal interface (light blue)	20
13	Component of a surface, from Ettl [16]	20
14	Mean height of the filtered segmented endosteal profile corresponding to Figure 11a regarding the cut-off frequency expressed relatively to the wavelength spatial frequency.	21
15	Segmented endosteal profile in red and filtered profile with industrial cut-off frequency (green) and the cut-off frequency determined for the bone (blue) corresponding to Figure 11a	22
16	Height profile regarding surface parameters	23
17	Emitted signal in temporal domain (left) and in frequency domain (right).	25
18	Initial map of the simulations, the bone is in yellow and the soft tissue and bone marrow are in blue.	26
19	Simulation map modeling the bone for various values of Rq , ρ_{length} , E_{Pore} , and d_{Pore}	27
20	Parameters for each simulation. All simulations are performed with ten values of Rq . The two firsts are performed on four values of ρ_{length} while the two last only on one. Parameters of porosity and the diameter of pores as one different value for each simulation	28
21	Simulation map for ten values of Rq ranging from 0.03 mm to 0.38 mm, and ρ_{length} from 0.5mm to 1mm, without pores (all maps are lined up to fit in the Figure)	29
22	Gamma distribution of the pore diameter. The parameters of the distribution vary regarding the patient, from Iori [23]	30
23	Generated realistic simulation map and post-process	31
24	Specularity map for $Rq = 0.23$ mm, $\rho_{length} = 2$ mm and $E.Pore = 0\%$. The Region of Interest, S.ROI, corresponding to the endosteum is within the red line	32

25	Mean Specularity over the lateral position $\overline{\psi_{\text{lateral}}}$. The value ranged from 0 to 1. Each case corresponds to the $\overline{\psi_{\text{lateral}}}$ of the map shown in Figure 21	33
26	Mean specular index in the S.ROI, $\overline{\psi_{\text{S.ROI}}}$, regarding Rq and ρ_{length}	35
27	Mean specular index in the S.ROI, $\overline{\psi_{\text{S.ROI}}}$, regarding Rq and ρ_{length}	36
28	Experimental setup for ultrasound acquisitions, the probe positioned on the sample, submerged in water, from Dia [14]	37
29	Parameters of the endosteal interface roughness interface for the 4 zones of interest of the three chosen femoral bones	42
30	Histogram of distributions	43
31	Gantt diagram	45

List of Tables

1	Parameters of Endosteal Interface Microstructure	22
2	Parameters of Intra-Cortical Microstructure	24
3	Variance (%) of the $\overline{\psi_{\text{lateral}}}$, rounded to two decimal places. Each case corresponds to the results of the corresponding simulation map in Figure 21	34
4	Pearson correlation coefficient regarding the surface parameters	34

Introduction

Osteoporosis is a bone disease affecting more than 200 million people worldwide, primarily causing loss of independence in individuals aged 50 and above [1]. It is characterized by the deterioration of bone microarchitecture, leading to a porous bone structure that increases its fragility and consequently increases the risk of fractures.

This fragility results from bone loss, a process balanced by continuous remodeling with bone formation and resorption phases. Osteoporosis disrupts this balance, leading to an excess of bone resorption over formation, therefore reducing bone mass.

This loss of bone mass occurs primarily in the cortical type of bone, predominant in the skeleton. Despite fractures occurring primarily in cortical bone regions, current methods for assessing bone loss quantify trabecular bone degradation. The second type of bone, with a spongy microstructure.

The Laboratory of Biomedical Imaging (LIB) has developed an ultrasound technique that enables cortical bone imaging. Traditionally used for soft tissue imaging, ultrasound is a non-invasive imaging method. This implemented method allows the observation of two osteoporosis biomarkers: bone density and thickness, both indicators of bone degradation.

Recent studies highlight that bone loss predominantly occurs at the intra-cortical surface near the bone marrow, known as the endosteum, leading to an increased porosity of the surface. Consequently, the surface roughness of cortical bone serves as an indicator of its degradation. The LIB proposed a bone imaging improvement, exploiting the properties of acoustical wave reflection on planar surfaces, to quantify surface roughness.

This study aims to quantitatively evaluate the roughness of the endosteal interface using these advanced ultrasound techniques.

The methodology is structured into four parts: firstly, an overview of the internship environment will be provided. Secondly, osteoporosis and the developed bone ultrasound imaging method will be presented. Thirdly, parameters defining the microstructure of the endosteal interface and determining its degradation state will be defined. Fourthly, the acoustic response concerning these parameters will be studied through simulations based on generated microstructures. Finally, future directions for this research will be discussed.

1 Internship environment presentation

The Biomedical Imaging Laboratory (LIB) is a public research institution specialized in fundamental and applied studies of morphological, functional, and molecular biomedical imaging techniques for both small animals and humans [2]. The LIB is under the tutelage of three organizations: Sorbonne University, the National Center for Scientific Research (CNRS), and the National Institute of Health and Medical Research (INSERM). It was established in 2014 through the fusion of two laboratories, the Laboratory of Parametric Imaging and the Laboratory of Functional Imaging. It is now located across two sites in Paris, corresponding to the former laboratory sites. The Cordelier site, adjacent to the Medical School, and the CHU Pitié-Salpêtrière, which house the medicine faculty and hospital. These proximate locations enable collaboration and innovation within the medical sphere.

The laboratory is directed by Lori Bridal and composed of permanent researchers, PhD students, and interns. The LIB comprises five specialized teams dedicated to various research domains:

- Ultrasonics and Imaging for Bone Quality Characterization (BQ)
- Development of Imaging and Targeted Therapy for Cancer and Inflammation (IT2D)
- Cardiovascular Imaging (iCV)
- Neural Connectivity and Plasticity (NCP)
- Physiology and Pathology of Microcirculation (PPM)
- 3D Mechanical Waves for Cardiovascular Imaging (OM3D), ATIP-Future

I did my internship in the BQ team. I was tutored during this internship by Quentin Grimal, director of the BQ team, and Amadou Dia, a PhD student finishing his thesis on the Quantitative ultrasound imaging of human cortical bone. The BQ team is dedicated to research in ultrasonic characterization and biomechanics of bone tissue, aiming to understand bone function and mechanical properties. Using both *in vivo* and *ex vivo* methodologies, the team develops ultrasound imaging techniques to characterize bone tissue. Their research aims to improve fracture risk diagnosis, especially among the elderly, and improve understanding of bone quality. The team's research is organized around three main projects: ultrasonic imaging of bone, assessment of bone quality in orthopedics, and development of laboratory methods for mechanical characterization of bone. During my internship, I participated in a project focused on ultrasonic imaging of bones [2].

2 Context and Approach of the Study

2.1 Introduction to the medical context: Osteoporosis

Osteoporosis is a bone disease that touches more than 200 million people, it is the primary cause of loss of independence in individuals aged 50 and above. This disease is characterized by microarchitectural bone deterioration, which results in porous bone structure, significantly escalating the risk of fractures due to increased fragility [1].

Within the skeleton, two types of bones exist: the trabecular which has a “spongy” microstructure, and the cortical bone, more dense, which represents nearly 90% of the skeleton. They have different properties and their repartition within the bone depends on the site as shown in Figure 2.

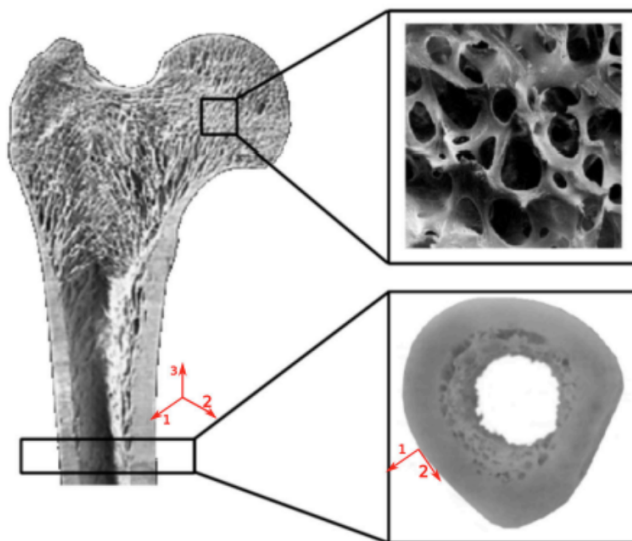


Figure 2: Structure of both types of bone, trabecular (top) and cortical (bottom).

Reproduced from Mouchet [3]

Healthy bones are constantly going through a process of remodeling with formations and resorptions phases. This process involves the action of two cells, the osteoclasts, responsible for bone resorption, and the osteoblasts, of bone formation. Additionally, osteocytes are involved in the initiation and control of bone remodeling [4]. Osteoporosis is characterized by an imbalance in the bone remodeling process, due to disrupted regulation of the three key cells involved. The resorption rate becomes thus higher than the formation one, leading to a reduction of the bone mass. This reduction alters the bone microarchitecture, the holes in the bone, or pores, are enlarged. This increase in porosity weakens the bone and makes it subject to more fractures.

Bone fractures are prevalent in cortical bone regions; in fact, 70% of bone loss occurs in cortical bone [5]. The medullary canal which contains the bone marrow within the cortical bone, is a site of high biological activity. Consequently, the activity of the three key cells involved in bone remodeling is higher in the bone marrow. This increased

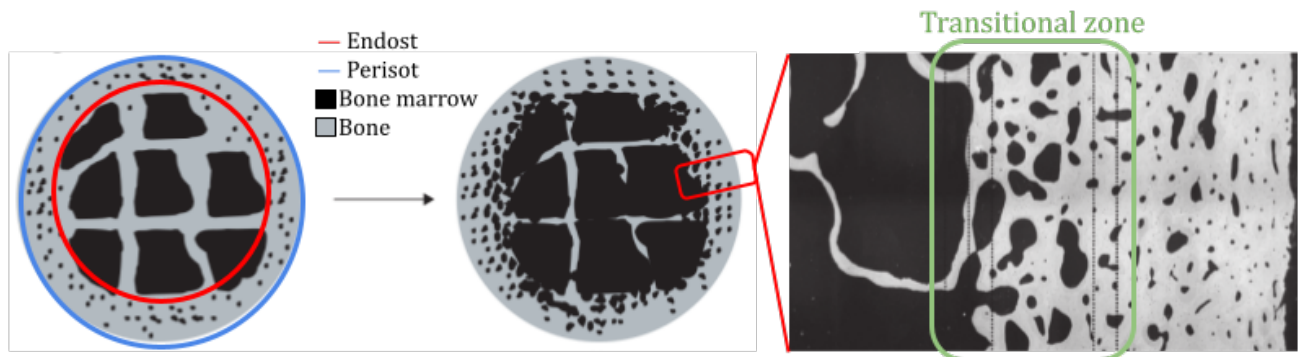


Figure 3: Bone degradation and transitional zone. Derived from Zebaze [5] [6]

activity means that the imbalance leading to bone degradation is more pronounced in bones located near the bone marrow. We can, consequently, observe a transitional zone (Figure 3) at the endosteum, the interface between the bone and the bone marrow, where the enlargement of pored appends primarily. Leading to a decrease in the density of the bone as well as its width [6].

However, bone mineral density (BMD) is presently the biomarker used to discriminate osteoporotic bone. It is measured with the Dual Energy X-Ray absorptiometry (DXA), considered the gold standard to evaluate the health of the bone and thus detect osteoporosis [7]. The BMD is evaluated in trabecular bone locations. The DXA technique isn't optimized for cortical bone architecture due to the low surface area compared to its volume. Therefore, variations in cortical bone are often not detected with this technique.

Given the significant impact of cortical bone loss on bone health, developing methods for assessing biomarkers of cortical bone health, such as its thickness and density, would improve our ability to diagnose and treat osteoporosis.

2.2 Basics of ultrasound imaging

Having discussed the physiological explanation of osteoporosis and introduced the concept of biomarkers, we now turn our attention to the methods used to assess bone health. In particular, we will focus on ultrasound imaging, a technique that has been used since 1984 for the diagnosis of osteoporosis [7]. Before explaining the specifics of how ultrasound imaging is used in bone health assessment, we will first provide a general overview of the principles of ultrasound imaging.

Ultrasound waves are acoustical mechanical waves of high frequency, typically between 2 and 20 MHz in the case of medical imaging applications. It allows us to visualize internal body structure by exploiting the properties of reflection of the ultrasonic waves.

The waves are emitted by transducers, which use the piezoelectric effect to convert an electrical signal into a mechanical one. The vibration of the transducer allows it to emit short pulsed waves into the medium and also to record the returning waves. These mechanical waves are reflected when they encounter a change in the impedance, related

to the density, of the medium, such as at the interface of organs or bones. The amount of reflected waves depends on the impedance difference between the two media. By analyzing the time at which the echo is recorded and its amplitude, we can reconstruct the position and density of objects. To generate 2D images in B-Mode (brightness mode) an ultrasound probe consists of multiple transducers, or elements. These elements allow control over the type of emitted wave by adjusting the delay between each element's emission. This control enables the transmission of planes or focused waves, for example.

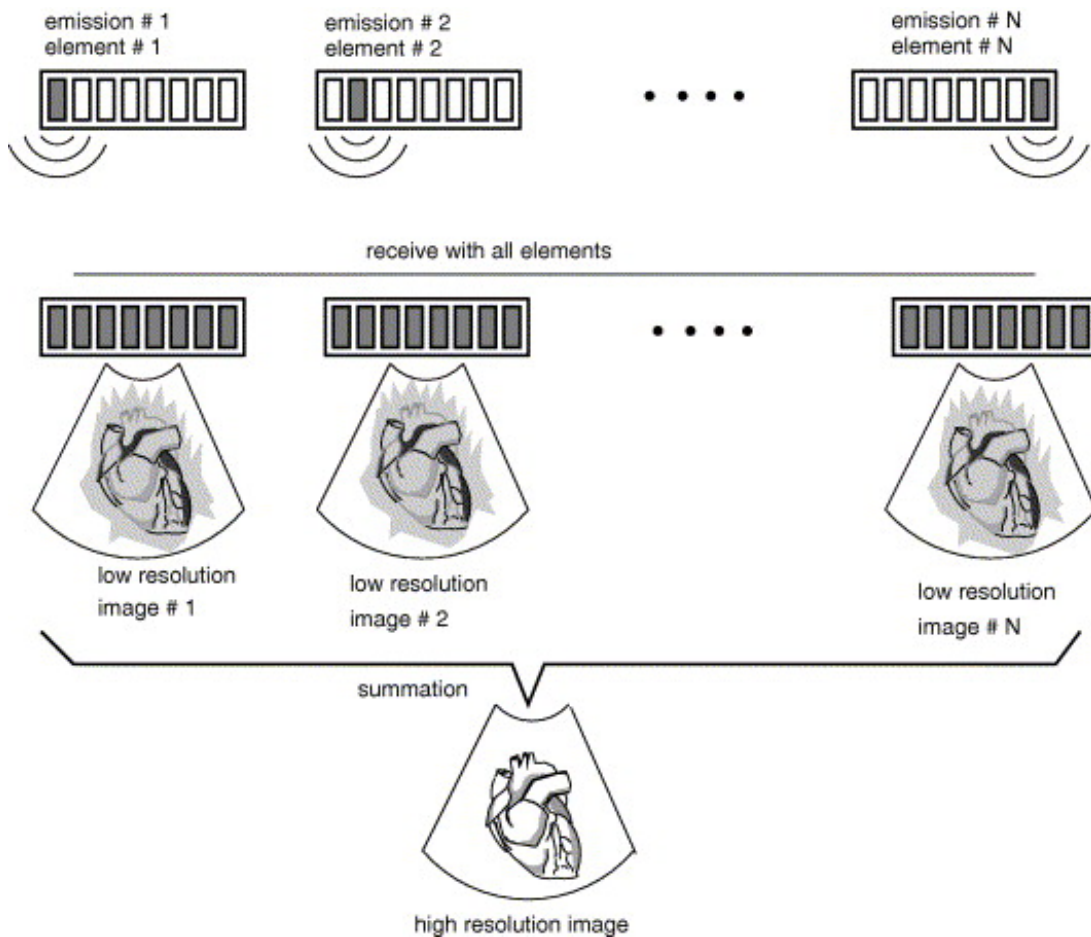


Figure 4: Basic principle of synthetic aperture ultrasound imaging, from Nikolov [8]

The study was performed with a programmable ultrasound probe (Vantage, Verasonics Inc., Redmond, WA, USA) probe. This probe is composed of 96 transducers operating at a central frequency of 2.5 MHz (P4-1 ATL/Philips, Bothell, WA, USA; pitch 0.295 mm), and the emitted pulse has an 80% bandwidth. This probe was operating in synthetic aperture mode [9]. In this mode, one element emits a wave, while all elements simultaneously record the back-reflected waves. Due to the properties of acoustic wave propagation, smaller emitting elements result in a wider range of propagation directions. Therefore, since the elements in our probe array are on the order of a few hundred micrometers, the emitted waves spread in all directions, meaning that all the medium will be insonified. Subsequently, a process of beamforming will be applied to reconstruct the images. This sequence of emission and reception is then repeated with each element emitting to reduce the signal-to-noise ratio and therefore increase the image quality, as in the

example Figure 4.

The beamforming process aims to combine the signal recorded for every single emission, and at each receiver, to reconstruct the ultrasound image. The beamforming method that we will study uses a delay and sum (DAS) algorithm [10]. The first assumption is that the speed of sound is homogeneous in all soft tissues, which constitute the majority of the human body, with a value of 1540 m/s. This first assumption also implies that the ray propagates in straight lines in the medium. The second is that the medium is composed of point-like objects that reflect the waves in all directions.

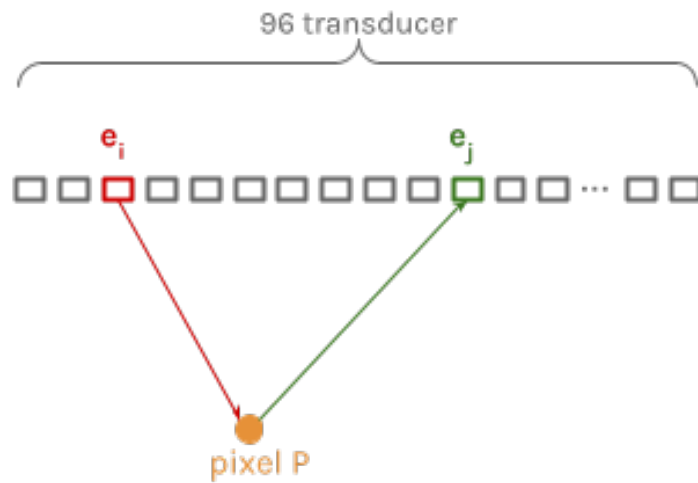


Figure 5: Ray-Path from emitter i to receiver i

The principle of the DAS algorithm functions by reconstructing each pixel P , Figure 5, of the imaged medium based on there travel time between an emitter i and each receiver j . The travel time refers to the duration it takes for the signal emitted by element i to reach element j after being reflected at a point within pixel P . Since the speed of sound c in the medium is uniform and known the travel time $\tau_{i,j}$ is linked to the distance by the relation:

$$\tau_{i,j} = c(d(e_i, P) + d(P, e_j))$$

With $d(e_i, P)$ the distance between the emitter i and the pixel P and $d(P, e_j)$ the distance between the pixel P and the receiver j .

Therefore the signal amplitude recorded by the element j that corresponds to the reflection on P of the signal from the element i is :

$$s_{i,j} = s_j(\tau_{i,j})$$

Where s_j corresponds to the signal recorded by the element j during the acquisition.

The beamformed signal for the element i , S_{BFi} , is therefore the sum of the signal received for each receiver j at the corresponding time $\tau_{i,j}$:

$$S_{BFi} = \sum_{j=1}^{Ne} s_j(\tau_{i,j})$$

with N_e the total number of elements, therefore 96 in our study.

This process is done for each pixel P to reconstruct the image of the emitting element i . The images from each emitter i are then summed to increase the image quality as explained before.

This technique is efficient for soft tissue, however, bones have highly different properties which challenges the traditional ultrasound imaging methods. Therefore, beam-forming method modifications are necessary to improve the imaging of cortical bones.

2.3 Principle of Bone Ultrasound Imaging

The material properties of bone make the classical DAS algorithm less effective for bone imaging. Therefore, adjustments are necessary to adapt the method for effective bone assessment.

2.3.1 Bone Imaging

The DAS beamforming algorithm assumes a homogeneous medium. However, bone has a higher density than soft tissue, resulting in an increased speed of sound within the bone. Additionally, the path of the sound waves is refracted at the soft tissue/bone interface. To address these issues, the DAS algorithm must be adjusted.

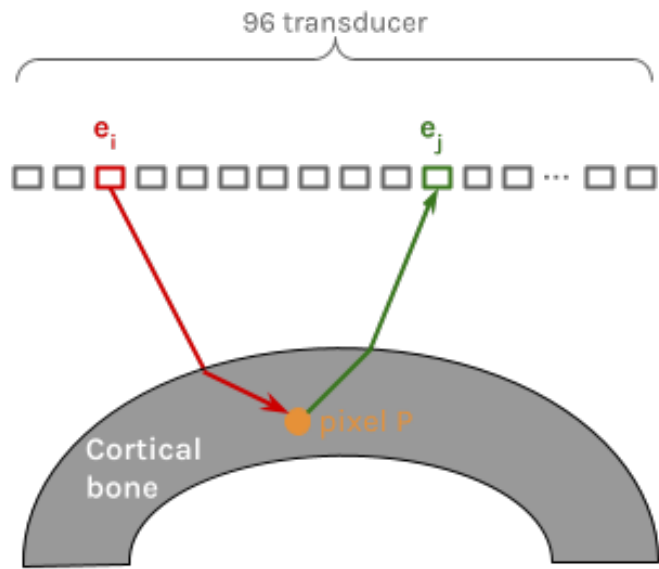


Figure 6: Ray-Path from emitter i to receiver j in homogeneous layers

In bone imaging methods, the medium is divided into homogeneous media considered anisotropic, with a homogeneous speed of sound. This assumption can be made because bones are isotropic in the transverse plane we will image. However, bones' speed of sound depends on their density and porosity. The speed of sound within the bone is $c_{bone} = 3500m.s^{-1}$ while it is $c_{softtissu} = 1540m.s^{-1}$. Therefore the mean speed

in the bone is reduced by the presence of pores. An autofocus method is employed to determine the speed of sound for each bone, based on the principle that the speed yielding the highest contrast corresponds to the speed of sound in the bone [11],[12].

The DAS algorithm is then applied as previously described for pixels above the periosteum. For pixels within the bone, the ray path and travel time are computed by accounting for the refraction effect (Figure 6), considering Snell-Descartes Laws. Additionally, the increased speed of sound within the bone is also considered. The endosteum is also segmented to consider a second refraction effect at this interface, to reconstruct proper pixels in the medullary cavity. This bone imaging technique was tested on healthy volunteers and proven effective. The experimental setup is shown in Figure 7. It allows us to obtain two bone parameters, bone thickness and density. These parameters are biomarkers of osteoporosis. However, this method requires the detection of both bone interfaces. Numerical simulations on ex-vivo bone indicate that large pores at the transitional zone near the interface make endosteum detection difficult [13].

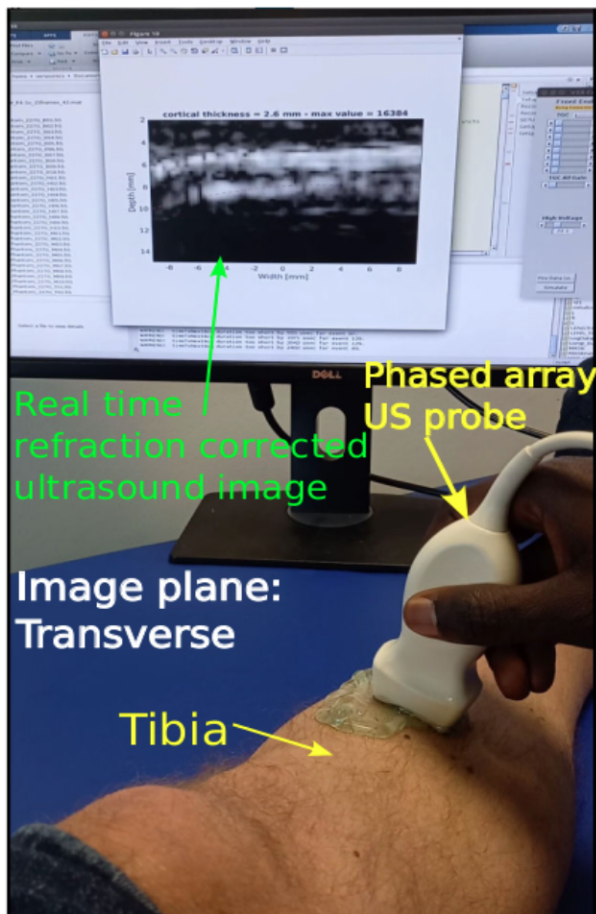
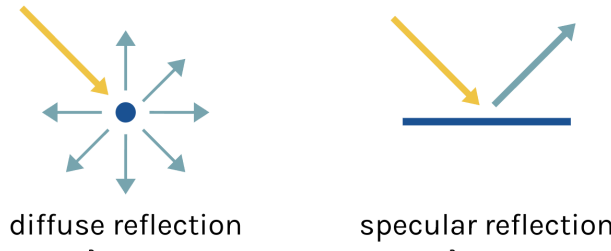


Figure 7: Setup for the acquisition of ultrasound data

These difficulties are linked to the reflection phenomenon of acoustic waves, which are influenced by the objects they reflect on. As shown in Figure 8a, an object with a significant size compared to the ultrasound wavelength will reflect the wave in a preferential direction, following Snell-Descartes' Law, resulting in specular reflection. On the other hand, an object considered small relative to the wavelength will reflect in all directions,

leading to diffuse reflection. The signal received by the ultrasound probe will therefore differ depending on the type of object encountered, as illustrated in Figure 8b. For simplicity, we will use the terms 'specular object' and 'diffuse object' to refer to objects that lead to specular or diffuse reflection, respectively.



(a) Reflection on objects of different size



(b) Receiving elements regarding the type of objects, from Dia [14]

Figure 8: Diffuse and specular acoustic responses

2.3.2 Specularity

In bone imaging, the bone interfaces are large compared to the wavelength, resulting in specular reflection. However, the presence of pores at the interface makes it rough, leading to more diffuse reflection. A method was thus implemented at the LIB, by my co-director Amadou S. Dia [14], to determine the contribution of diffuse or specular reflection on the received signal, thus quantifying the smoothness of the interfaces.

To quantify the specularity within the imaged medium, the specular index was introduced. It is determined by calculating, for each pixel, a normalized correlation between a model of the signal received from a perfectly specular object (Figure 9a) and the actual signal, known as the specular transform [15]. The specular transform corresponds to the recorded signal $s_{i,j}$ for each mid-angle β . The mid-angle β is an average of the incident angle, between the emitter and the pixel P, and the reflected angle, between the pixel P and the receiver. For instance, consider the pixel indicated by the red triangle, which is either on a specular or diffuse object (Figures 9b and 9c). The normalized correlation of the model with the respective specular transform (Figure 9d and 9e) reaches a maximum closer to 1 when the surface is specular (Figure 9f) compared to when it is diffuse (Figure 9g). This maximum correlation value is defined as the specular index ψ , quantifying the contribution of specularity at the pixel location.

The beamforming process can be adapted to incorporate the specular reflection of

surfaces based on the specular index. This method enhances the quality of reconstructed bone images.

This study aims to investigate specular reflection, building on the findings of Amadou S. Dia [14], particularly at the intra-cortical interface. It aims to assess the quality of the inner interface of cortical bone using the specular index as an indicator. This metric can quantify the transitional zone at the endosteal interface, potentially serving as a new biomarker for assessing bone health.

Our research question is how does the specular index ψ behave with respect to bone microstructure? The first step is therefore to accurately define the microstructures of the endosteal interface through a parametric study, followed by analyzing the specular index's dependence on each parameter.

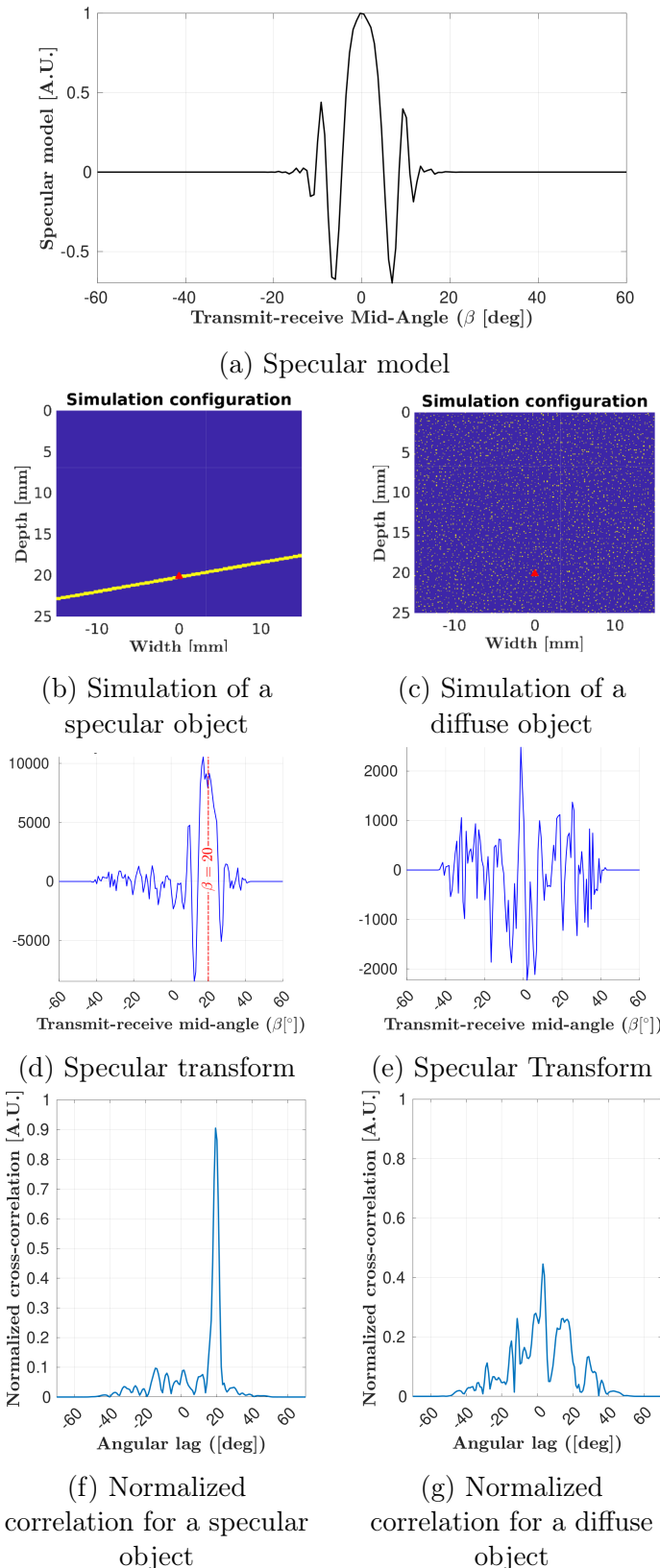


Figure 9: Diffuse and specular acoustic responses (d) and (e) of different profiles (b) and (c). Correlation (f) and (g) of the acoustic response with the specular model (a), from Dia [14]

3 Ex-Vivo Bone Parametric Study

To evaluate the specular response of the endosteal interface and quantify its degradation, we must establish quantifiable parameters that effectively describe its microstructure. We aimed to characterize the transitional zone, as explained in the section 2.1, to determine the health state of the bone. The bones studied are considered healthy when the bone is compact near the interface between the bone and bone marrow and the endosteal interface is relatively smooth when visually observed. In contrast, they are considered unhealthy if there are large pores near this interface and a rough endosteal interface which indicates degradation. Although surface roughness parameters have been studied, they have not been characterized within the context of bone. This research aimed to describe the endosteal interface to subsequently analyze its acoustic response in relation to these parameters.

3.1 X-Ray Ex-Vivo Images

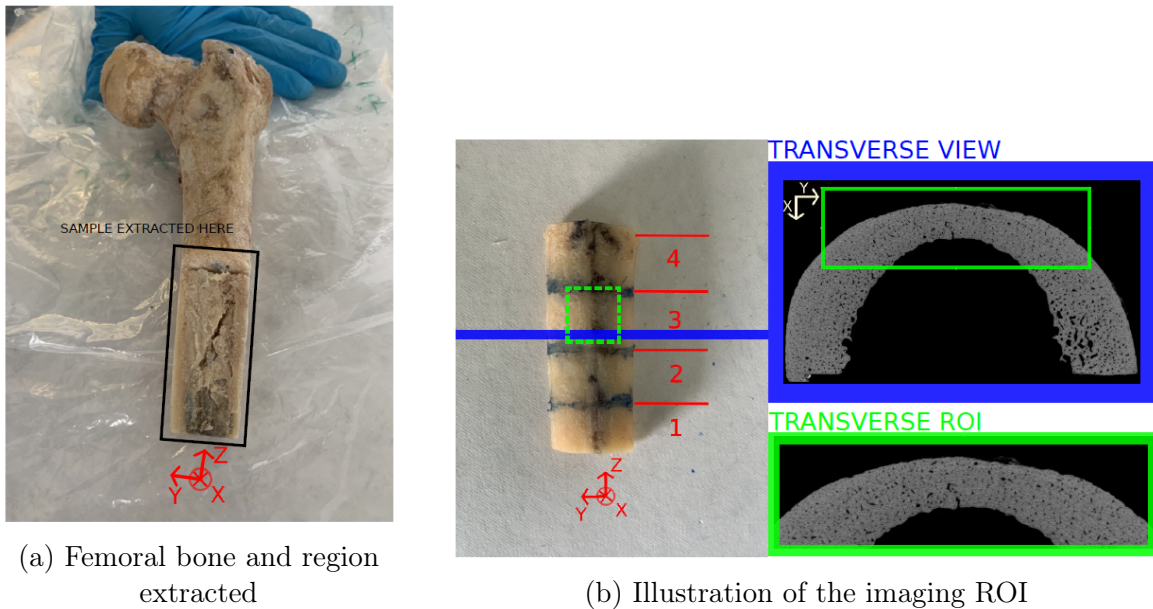


Figure 10: Bone extraction and region of interest that is going to be imaged, from Dia [14]

Parameters were evaluated through image processing on computed tomography scan (CT-scan) ex-vivo bone images from three femoral bones (Figure 10a). CT scans, an X-Ray imaging method, were acquired in the transverse plane of cortical bone, with a resolution of $9\mu\text{m}$. The analysis focused on a region of interest (ROI) as depicted in Figure 10b. The scans were performed at IMOSAT (Université Paris Descartes). The setup includes a micro-CT system (Skyscan 1176; SkyScan-Brücker, Kontich, Belgium) with a scintillator connected to a CCD Princeton camera. The camera had a pixel size of $12.53\ \mu\text{m}$ and captured images in 16-bit depth.

We aimed to characterize the endosteal interface, highlighted in red in Figure 11. Due to the resolution limitations of ultrasound in bone, as shown in Figure 12, the

detected endost that corresponds to the bone in Figure 11b has a width of approximately 2 mm. Therefore, it will not be distinguished from the blue area within one wavelength of the endosteum (Figure 11). The blue region will be denoted as the endosteal intra-cortical region of interest (E.ROI). The parameter determination for these two regions will be illustrated using the example of the bone shown in Figure 11a.

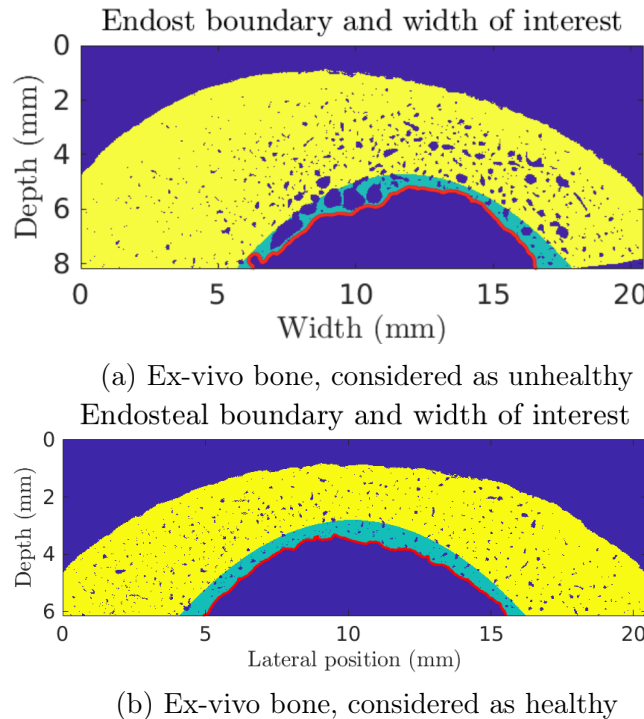


Figure 11: Ex-Vivo Bone and delimitation of the endosteal interface (red) and the E.ROI (blue)

3.2 Analysis of the endosteal interface microstructure

We will determine parameters for the endosteal interface by focusing on the image processing method employed and the parameters chosen.

3.2.1 Image processing method

The segmented endosteal interface (highlighted in red in Figure 11a) within the ROI has a parabolical shape unique to each bone. We employed an industrial approach to normalize the computation of parameters at the endosteal interface. Profiles are composed of three components related to their spatial frequency, as illustrated in Figure 13 [16].

The parabolical shape of the bone corresponds to the component with the lowest spatial frequency, thus the form. A high-pass filter would therefore allow us to obtain the components of interest [17] [16]. To extract the roughness and the sum of the waviness and the roughness components of the profile, we need to determine the cut-off frequency of the highpass filter.

The usual cut-off frequency to isolate the roughness profile as defined industrially

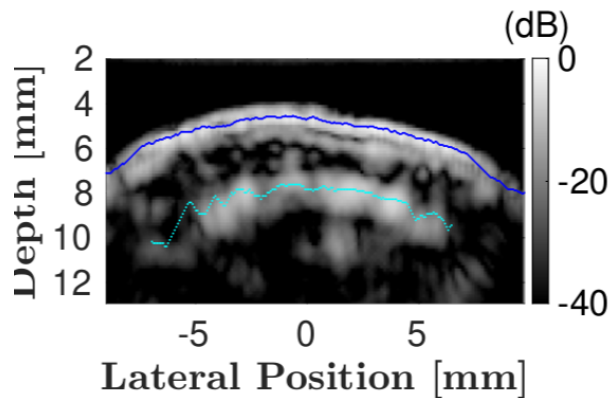


Figure 12: Resolution of the specular beamformed image, with the periosteal interface (deep blue) and the endosteal interface (light blue)

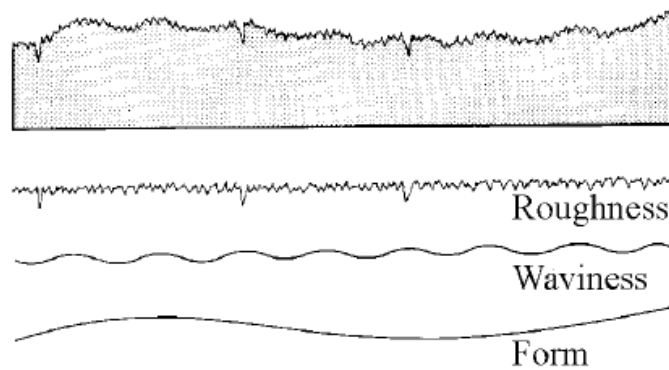


Figure 13: Component of a surface, from Ettl [16]

is a frequency that corresponds to a pattern of 0.8mm, thus a frequency $k_{industry} = 1.25\text{mm}^{-1}$ [16]. The acoustical wavelength in the bone is of the order of a millimeter. For instance, for the bone in Figure 11a, the speed of sound is 1.28 mm (the formula is detailed in the next paragraph), while it is 1.38 mm for the bone in Figure 11b where the speed of sound is higher as it is less porous. Consequently, the ultrasound resolution does not allow to observe the roughness profile of the endosteal interface, in green in Figure 15, where variations are of the order of $10\mu\text{m}$. This roughness profile will appear as smooth in the imaging process. Since variations in the industry are smaller than the ones we observe in bone degradation, the roughness as defined in the industry would correspond to a combination of roughness and waviness in the bone context, which we will refer to as waviness.

Consequently, the surface parameter will be computed on the waviness. To determine the appropriate cut-off frequency, we computed the mean height of the profile for various values. When the mean height is equal to zero, we can estimate that the parabolic form of the bone has been filtered, isolating the waviness components.

We plotted the mean height against the spatial wavelength frequency to give significance to our results. For the chosen sample, the average speed has been estimated to be $c_{bone} = 3200 \text{ m s}^{-1}$ [14]. The corresponding wavelength and spatial frequency are

consequently

$$\lambda = \frac{c_{\text{bone}}}{f_{\text{probe}}} = \frac{3200 \text{ m s}^{-1}}{2.5 \times 10^6 \text{ Hz}} \approx 1.28 \times 10^{-3} \text{ m} \approx 1.28 \text{ mm} \Rightarrow k_\lambda = \frac{1}{\lambda} = \frac{1}{1.28} \approx 0.78 \text{ mm}^{-1}$$

. We therefore express the frequency as a fraction of k_λ in Figure 14.

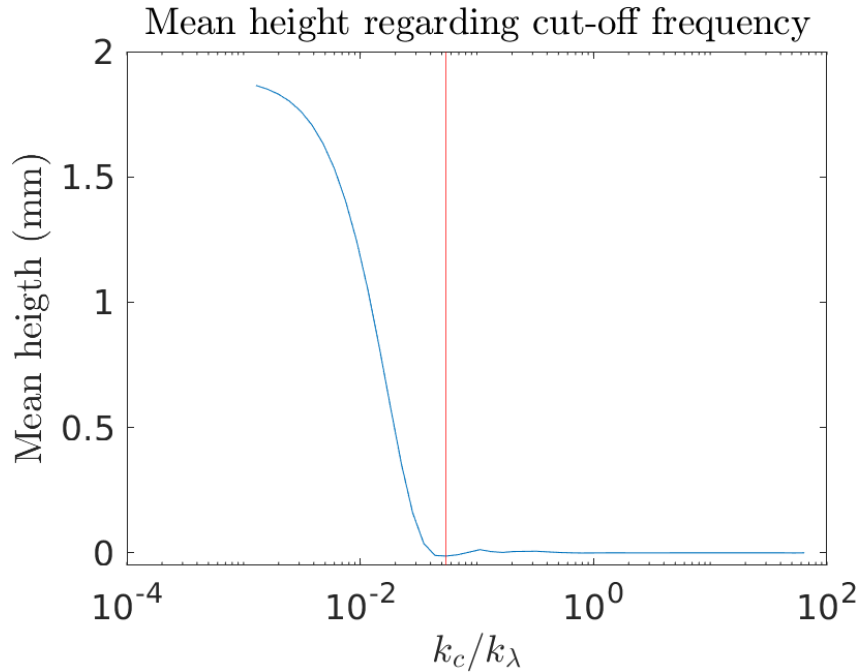


Figure 14: Mean height of the filtered segmented endosteal profile corresponding to Figure 11a regarding the cut-off frequency expressed relatively to the wavelength spatial frequency.

As shown in Figure 14, the cut-off frequency for this bone microstructure is, therefore, $k_c \approx 0.055k_\lambda \approx 0.043 \text{ mm}^{-1}$. This cut-off frequency is employed in a high-pass filter is applied to the original segmented profile in red in Figure 15 to obtain the waviness in blue.

This filtering allows us to focus on the variations in the profile that are not due to the original form of the bone, and that therefore represent the roughness of the endosteal interface. Consequently, the surface parameters can be accurately computed on the filtered profile.

3.2.2 Parameters definition

Existing literature suggests that surface roughness can be effectively quantified by evaluating the root mean square of height (Rq) relative to a planar surface, along with the correlation length of height (ρ_{length}) [18]. Moreover, these parameters are relevant in the context of ultrasound imaging, as previous investigations indicate that the Rq decreases the specular response of surfaces [19], [20]. However, these parameters have not been characterized within the context of bone.

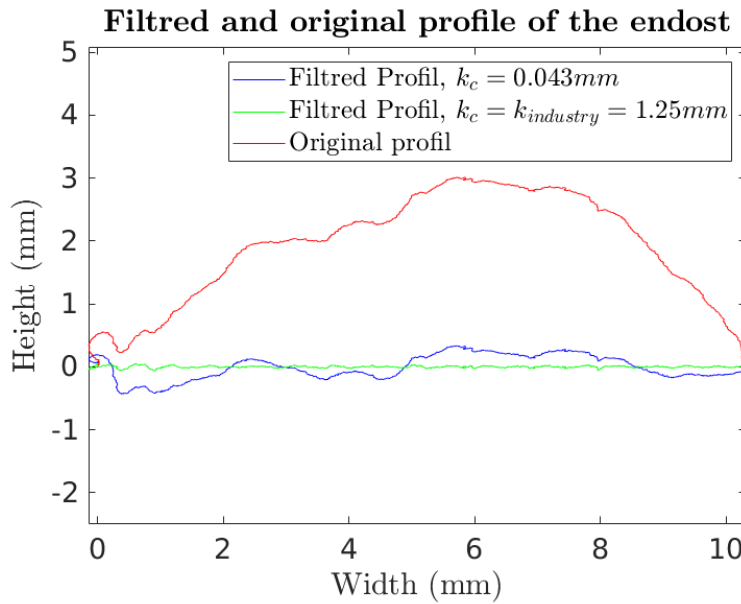


Figure 15: Segmented endosteal profile in red and filtered profile with industrial cut-off frequency (green) and the cut-off frequency determined for the bone (blue) corresponding to Figure 11a

The Rq expresses the mean height variation compared to a smooth surface. It therefore gives insight into the amplitude of the height variation. As shown in Figure 16b and 16c, a higher Rq induces a higher variation of the height surface and therefore a rougher surface. However, this parameter alone does not fully describe a surface, as surfaces 16a and 16b can have the same Rq . Therefore we introduce a second parameter, the ρ_{length} . The ρ_{length} corresponds to the distance at which the auto-correlation function of the profile is equal to $1/\exp(1)$.

This parameter characterizes the abruptness of changes in the profile. This indicates the distance over which height variations occur. A longer ρ_{length} means smoother transitions, while a shorter one indicates more abrupt changes. As illustrated in Figures 16a and 16b, a higher ρ_{length} results in a smoother profile.

In summary, the profile becomes smoother as the Rq decreases and the ρ_{length} increases. The comparison of parameters between the example of a degraded bone (Figure 11a) and a healthy bone (Figure 11b) confirms the relevance of the chosen parameters. The results in Table 1 demonstrate that the healthier bone has a lower Rq and a higher ρ_{length} , validating our approach.

Bone Condition	Rq [mm]	ρ_{length} [mm]
Degraded bone	0.20	1.240
Healthy bone	0.16	2.040

Table 1: Parameters of Endosteal Interface Microstructure

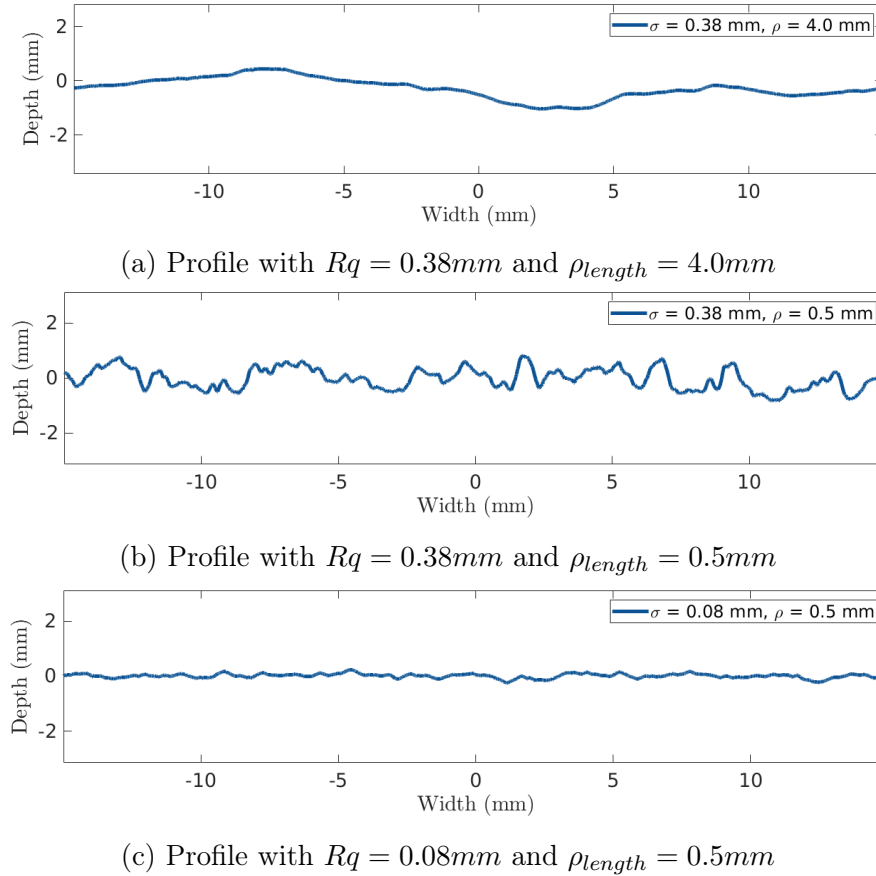


Figure 16: Height profile regarding surface parameters

3.2.3 Analysis of the intra-cortical micro-structure

Given that ultrasound wavelengths are on the order of a millimeter, the surface description doesn't encompass the characteristics of the region identified as the endosteal interface by ultrasound. Especially as ultrasound imaging contrast is highly influenced by intra-cortical microstructure such as pore size and porosity [13]. We will determine these parameters in this study by focusing first on the image processing method employed and then on the choice of parameters.

The region studied, E.ROI, shown in blue in Figure 11a, is within $\lambda = 1.28\text{mm}$ of the endosteal surfaces. To select this region, a parabola was fitted to the segmented endosteum and then expanded using the properties of parabolas. Porosity was computed on the binarized CT-scan image by calculating the ratio of pixels corresponding to soft tissues (i.e., pores) to the total number of pixels between the endosteal boundary and the expanded parabola. This volume ratio, denoted as $E.Por$, is expressed as a percentage of porosity, as shown in Table 2. The second parameter assessed was the mean pore size within the blue area. The boundaries of the pores were segmented, and the approximate centers of the pores were computed. Pores were considered to be in the endosteal zone if their centers were located within the blue area. Assuming the pores are round, their perimeter was determined based on the number of pixels in the segmented pores. The diameter was then calculated using the formula: diameter = $\frac{\text{perimeter}}{\pi}$. The parameter

chosen to describe the bone is the mean diameter within the E.ROI, denoted as $d.Pore$. The parameters reflect the actual conditions, with healthy bone exhibiting nearly six times lower porosity and smaller pore diameters.

Bone Condition	Porosity $E.Pore$ [%]	Pore diameter $d.Pore$ [mm]
Degraded bone	32.3	0.41
Healthy bone	5.3	0.13

Table 2: Parameters of Intra-Cortical Microstructure

This study allowed us to characterize the endosteal interface microstructure by analyzing CT-scan images of ex-vivo femoral bones. We established that the rugosity of the endosteal interface is characterized by key parameters such as Rq and ρ_{length} , which assess surface description. Additionally, we evaluated intra-cortical microstructure, including porosity and pore size, in a region close to the endosteal interface, E.ROI. The relevance of these parameters was validated by the comparison of the two healthy and unhealthy bones, shown in Figure 11. The parameters were also computed for the last bone and the four zones, the results are shown in Appendix A.

4 Analysis of the endosteal interface specular response, a simulation study

To understand the relation between the bone microstructure and its acoustic response, we need to evaluate the specular response for each parameter individually. This can be done by simulating the imaging sequences on generated profiles and changing one parameter at a time. Simulation possesses advantages compared to ex-vivo and in-vivo experiments, such as the elimination of interactions with surrounding elements, enabling a more accurate analysis of the effects of each parameter.

4.1 General parameters of the simulation

The simulation was performed with the open software Simsonic [21] ⓒ. SimSonic is a Finite-Difference Time-Domain (FDTD) code used to simulate elastic wave propagation in media, including bone and soft tissue. The parameters of the medium, the probe, and the generated signal are taken as input by the software. In our cases, we simulated under the same conditions as the experimental measurement performed in the LIB. Therefore we modeled a linear array made of 96 elements. The imaging sequence is a synthetic aperture one, with each element emitting a short pulse which is a Gaussian-windowed tone burst with a central frequency of 2.5 MHz as shown in Figure 17.

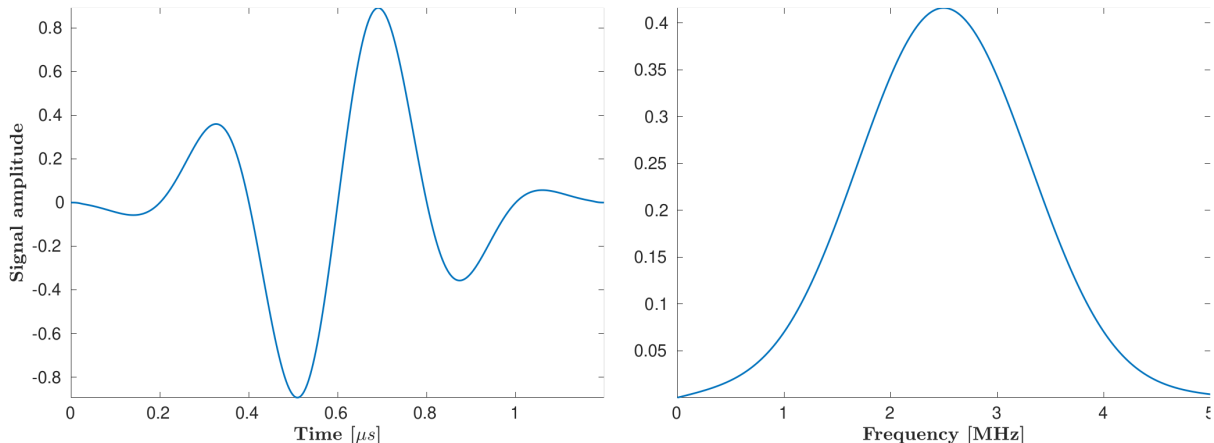


Figure 17: Emitted signal in temporal domain (left) and in frequency domain (right).

To model the layered medium through which the waves propagate, we defined a spatial step of $\Delta x = 10\mu m$. This value satisfies the convergence condition of the FDTD model, which allows the accuracy of the model. The depth of the medium is set at 15 mm and the width at 30 mm for all simulations.

The material properties are specified by the speed of sound and the elasticity of the medium. In our case, to mimic both soft tissues and bone marrow, we used a speed of sound of $V_{\text{soft tissu}} = 1540m/s$ and defined the medium as a fluid with a density of 1 mg/mm^3 . The second layer, which mimics bone, has a speed of sound of $V_{\text{bone}} = 3500m/s$ and is an elastic medium with a density of 2 mg/mm^3 .

The probe is immersed in the first layer, corresponding to the soft tissue, at a

depth of 2 mm. The periosteal interface is located at 5mm in the medium, and the endosteal interface is at 10mm. Therefore we have a 5mm thick bone. The two surfaces are planar to simplify the problem as shown in Figure 18.

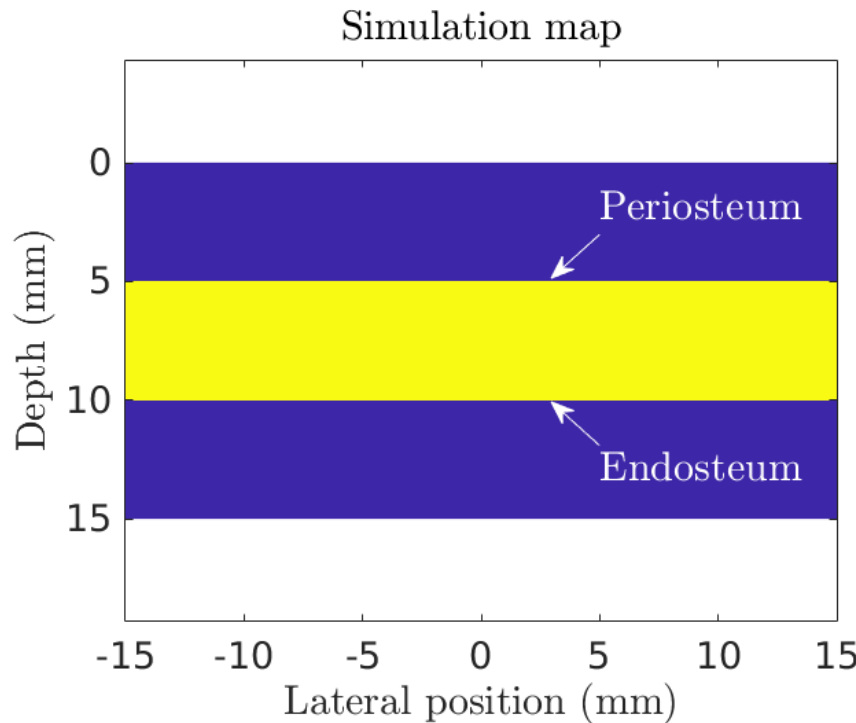


Figure 18: Initial map of the simulations, the bone is in yellow and the soft tissue and bone marrow are in blue.

The simulation models wave propagation through the medium. The output is a temporal signal for each receiving element, containing information about the time of signal reception and its amplitude. To evaluate the specular response regarding the bone microstructure, all parameters will remain constant, to focus on the generation of layered media that mimics the bone.

4.2 Generation of bone micro-structure model

4.2.1 Generation of simple microstructures

Having established the simulation parameters, the next step is to generate realistic surface profiles that accurately represent the bone interface.

Generation of surfaces

Surfaces with the appropriate Rq and ρ_{length} are generated using statistical formulas. The number of points generated corresponds to the length of the simulation map, calculated as the length divided by the step size. For our case, with a map length of 30 mm and a step size of $\Delta x = 10\mu m$, we need to generate a surface 3000 pixels long. This step size was chosen to match the resolution of the ex-vivo images obtained by CT scan, ensuring consistency in parameter computation. First, the height of each pixel is generated from a

normal height distribution with a standard deviation equal to the desired Rq . To obtain the desired ρ_{length} , a Gaussian filter is applied. This filter smooths the surface to obtain the desired ρ_{length} [22]. The Gaussian filter's shape is defined by an exponential decay function:

$$F(x) = \exp\left(-\frac{|x|}{\rho_{\text{length}}/2}\right)$$

where x represents the distance from the center.

This method introduces randomness, the filter can overly reduce the Rq . Consequently, the profile has a lower Rq than desired. To address this issue, surfaces were re-generated while the calculated Rq and ρ_{length} deviated by more than 10% from the desired value.

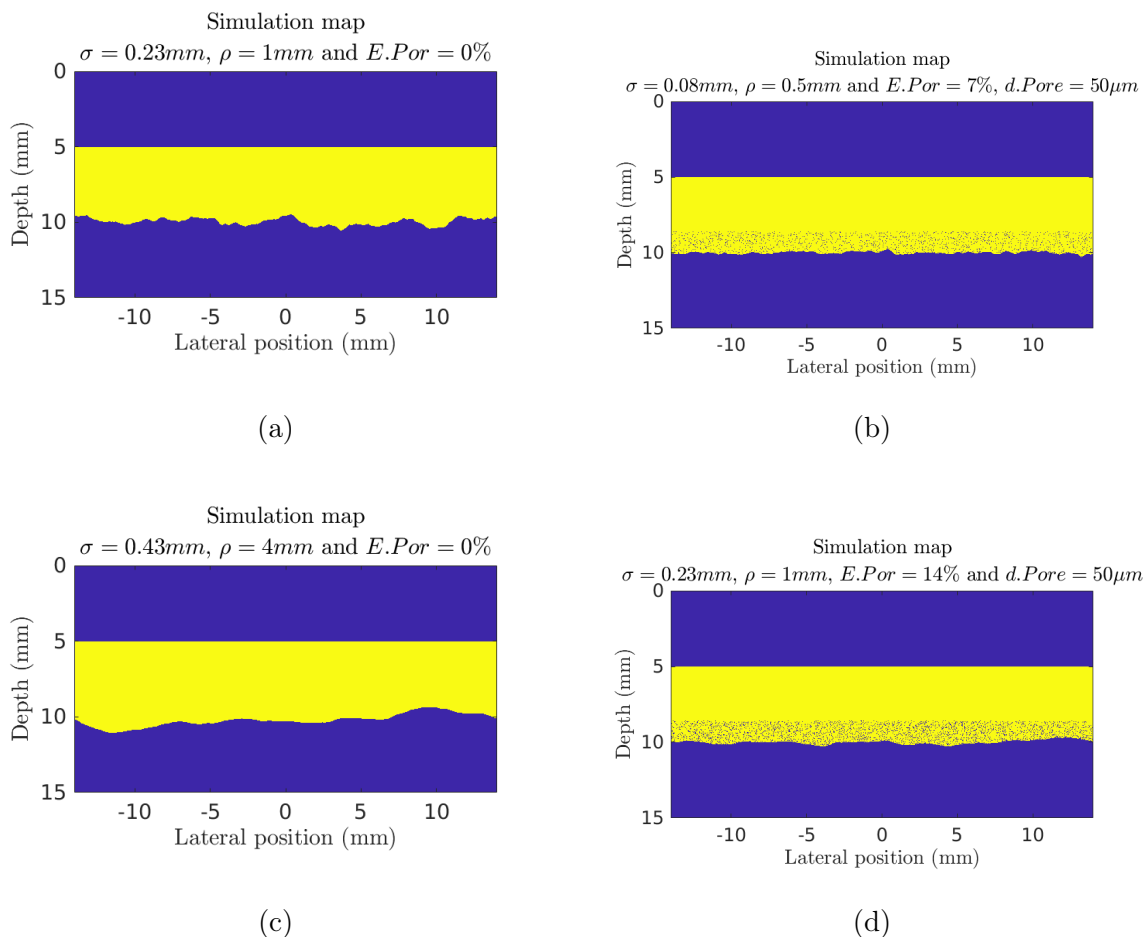


Figure 19: Simulation map modeling the bone for various values of Rq , ρ_{length} , E_{Pore} , and d_{Pore}

Introduction of porosity

Porosity was introduced in a one wavelength width above the endosteal interface, thus in the E.ROI. Since we are interested in this region, we didn't add pores in all the depths of the interface. The pores were iteratively added while the porosity in the one wavelength

width wasn't reached. To simplify the computational time, we only added one size of pore per simulation map. We studied without pores and with 2 values of porosity as well as two values of diameters of the pores.

Various profiles generated from various parameters describing both the endosteal surface and the E.ROI are depicted in Figure 19

Generation of the map for each simulation

The first simulations were performed on four values of ρ_{length} and ten of Rq , with pores and without pores at 7% of porosity and pores of diameter $50\mu\text{m}$. They correspond to simulations N°1, shown in figure 21, and simulation N°2 in Table 20. Therefore, eighty simulations were performed. It is important to note the simulation time of approximately 2 hours for one simulation. Due to the length of the simulations, there was a need to select the varying parameters. Following the initial results, we decided to maintain a single value for the correlation length, $\rho_{\text{length}} = 2\text{mm}$. Simulations with a porosity of $E.Pore = 14\%$ and a diameter of pores $d.Pore = 100\mu\text{m}$ were performed on 10 maps each, using 10 different values of Rq . These parameters are shown in the Table 20.

Simulation N°	Rq [mm]	ρ_{length} [mm]	E.pore [%]	d.Pore [mm]	Number of simulations
1	0.03	0.5	0	0	40
	0.08		7	0.05	40
	0.13		7	0.1	10
	0.18		14	0.05	10
2	0.23	2	7	0.05	40
	0.28		7	0.1	10
3	0.33		14	0.05	10
	0.38				
	0.43				
	0.48				

Figure 20: Parameters for each simulation. All simulations are performed with ten values of Rq . The two firsts are performed on four values of ρ_{length} while the two last only on one. Parameters of porosity and the diameter of pores as one different value for each simulation

By processing the recorded signals from each simulation, we aim to isolate and understand the specific effects of each parameter on the specular response.

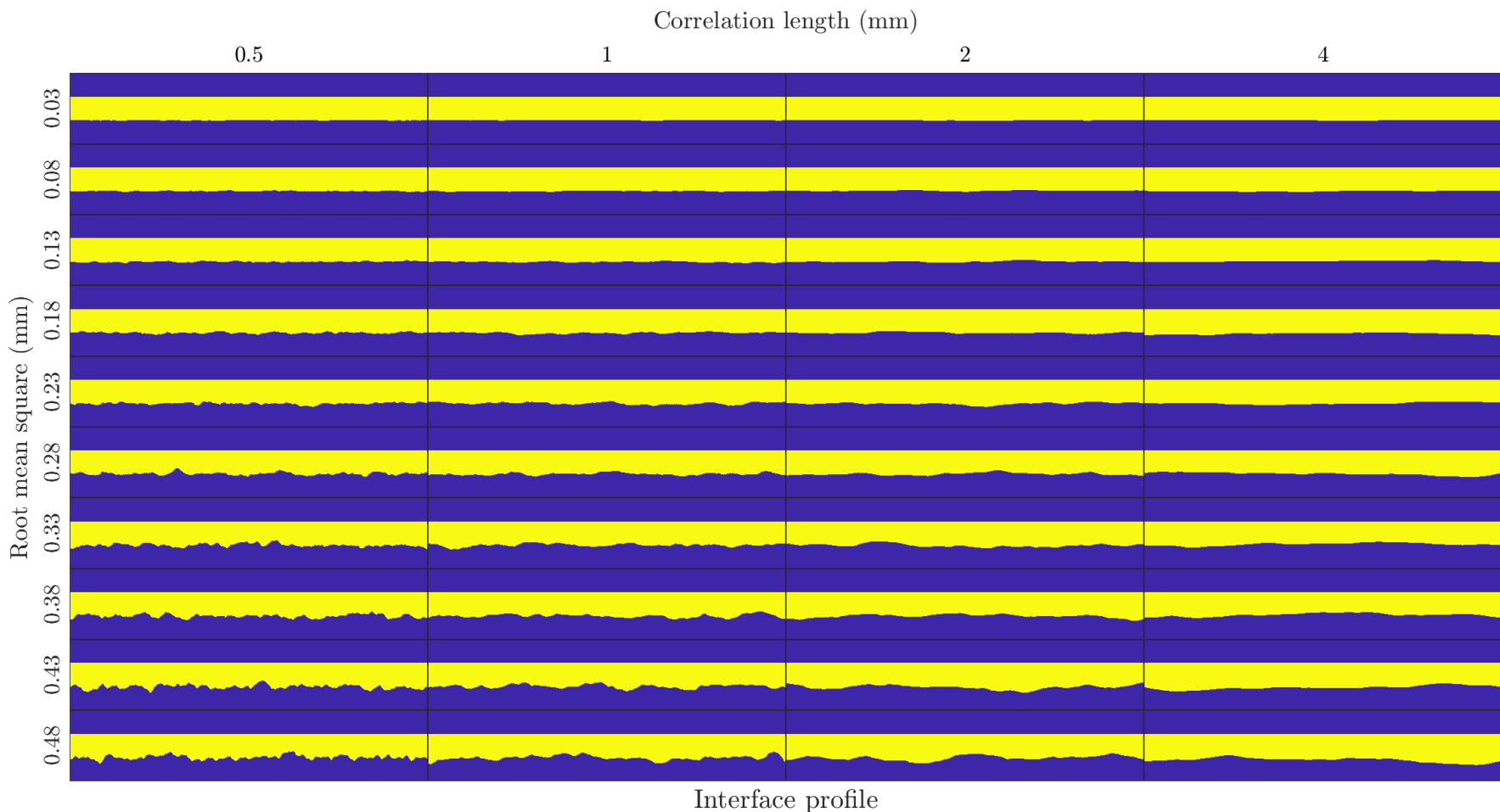


Figure 21: Simulation map for ten values of Rq ranging from 0.03 mm to 0.38 mm, and ρ_{length} from 0.5mm to 1mm, without pores
 (all maps are lined up to fit in the Figure)

4.2.2 Generation of realistic microstructures

The microstructure generated for the initial simulations has limitations such as the uniform size of pores, and the uniform position within a one-wavelength-wide band above the endosteal interface. Studies of the bone have shown that the diameter of bone pores follows a gamma distribution with the parameter α and β that varies regarding the type of patient (young, aged, or osteoporotic), as shown in Figure 22 [23].

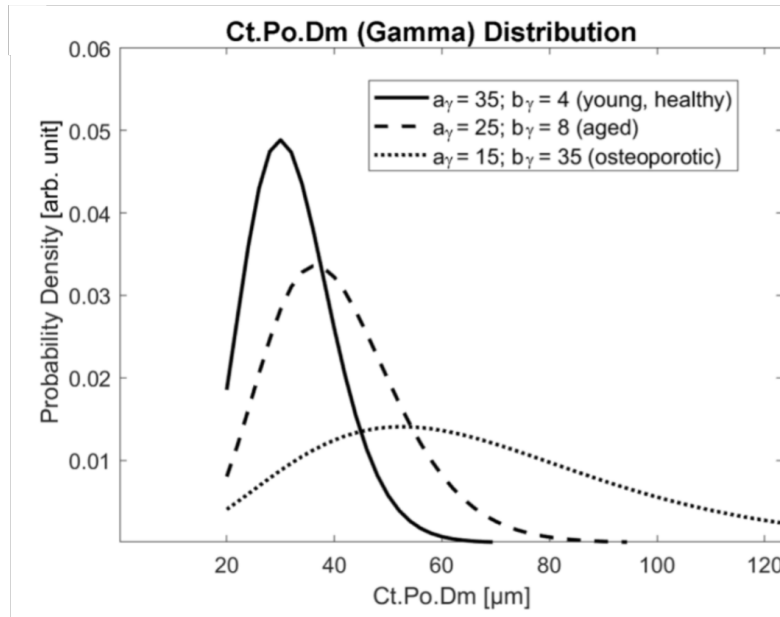


Figure 22: Gamma distribution of the pore diameter. The parameters of the distribution vary regarding the patient, from Iori [23]

Furthermore, the distribution of pore positions along the depth of the bone is not homogeneous. We, therefore, introduce a Gaussian distribution of the pores along the depth of the bone, or the z axis. This distribution is centered around the endosteal boundary, at a depth $\mu = 10mm$, and the full width at half maximum (FWHM) corresponds to twice the wavelength in the bone $2 * \lambda_{\text{bone}} = 2 * 1.4mm = 2.8mm$ when we consider the speed of sound in a bone without pores thus $V_{\text{bone}} = 3500m/s$. The standard deviation of the Gaussian distribution is related to the FWHM by the formula $\sigma = \frac{\text{FWHM}}{2.35} = \frac{2.8}{2.35} \approx 1.2mm$ Conversely, the position of the pore along the lateral position, or the width x , is uniformly distributed.

To sum up,

- the x position of the pores follows a uniform law: $x \sim \mathcal{U}(0, 30)$,
- the z position of the pores follows a gaussian law: $z \sim \mathcal{N}(10, 0.06^2)$
- the diameter of pores $d.Pore$ follows a gamma distribution $d.Pore \sim \Gamma(\alpha, \beta)$ with, (α, β) that varies regarding the bone.

To generate the surfaces, we iteratively determined the positions and diameters of

pores until the desired porosity was reached. Each position (x and z) and pore diameter ($d.Pore$) are chosen according to these distributions.

For example, for a 30% porosity, we obtain the simulation map shown in Figure 23a. The histogram of the position and the diameters of the pores are shown in appendix B. To increase the realism of the simulation map, a Gaussian filter with a standard deviation of 2 is applied, as illustrated in Figure 23b. This choice of standard deviation is validated by comparing results with actual bone microstructures. We observe unconnected bone pixels, circled in red, as this configuration isn't physiologically possible, we filtered the unconnected objects, as shown in Figure 23c.

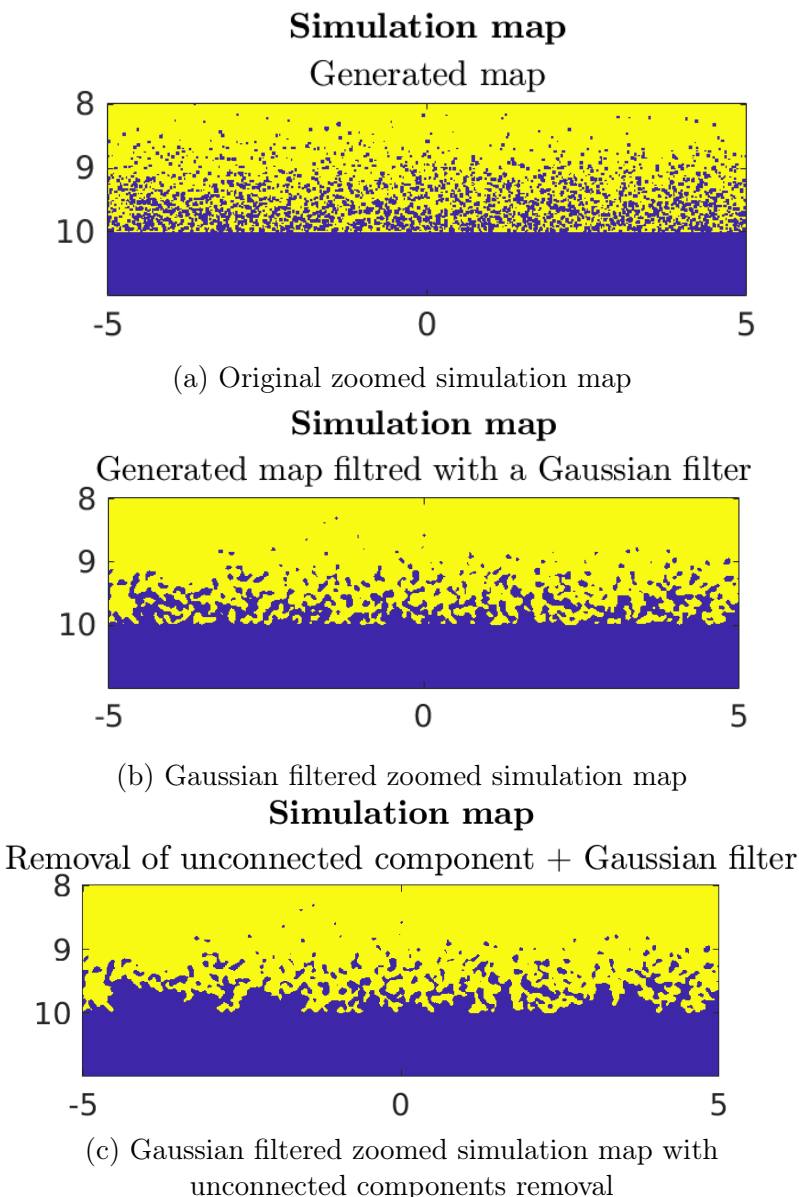


Figure 23: Generated realistic simulation map and post-process

This process allows us to achieve a realistic bone microstructure. However, con-

trolling the parameters is more complex compared to simpler microstructures. As a result, analyzing the influence of each parameter becomes more precise with the previously generated microstructure. The analysis of more complex microstructure can be directly obtained from ex-vivo images of the bone (see Perspective 5). Consequently, we didn't simulate the propagation of ultrasound waves on these maps.

4.3 Post-process of the simulation and analysis of the results

4.3.1 Post processing of the simulations

We apply the specular method as previously explained to study the specular echoes from the surfaces regarding each parameter. We apply the process explained in part 2.3.2 to create a specular map. For example, in the simulated map shown in Figure 19a, we obtain the specular map depicted in Figure 24. The periosteum, at 5 mm, is perfectly specular, resulting in a specular index ψ close to 1. Conversely, the specular index for the endosteum, at 10 mm, is closer to 0.5 due to its rougher interface.

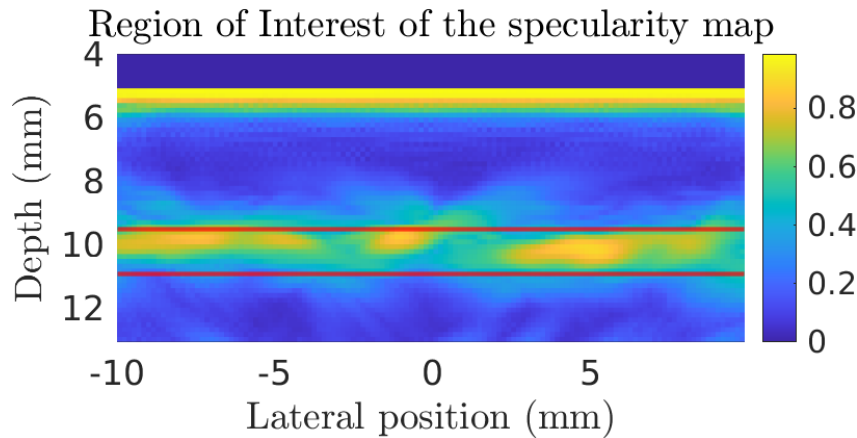


Figure 24: Specularity map for $Rq = 0.23 \text{ mm}$, $\rho_{length} = 2 \text{ mm}$ and $E.Pore = 0\%$. The Region of Interest, S.ROI, corresponding to the endosteum is within the red line

To quantify the specular response of the endosteal interface, a region of interest (S.ROI) was selected. The S.ROI is a one-wavelength-wide centered around the estimated endosteal position, at a depth of 10mm, as shown in Figure 24. To analyze the specular response along the lateral position, the specular index was averaged for each column within the S.ROI, providing the mean specular index for each position X , $\bar{\psi}_{\text{lateral}}$, as shown in Figure 25. The variation amplitude within each simulation map was also evaluated by computing the variation of the $\bar{\psi}_{\text{lateral}}$. Additionally, the mean specular index across the entire S.ROI was calculated to provide a single metric for each simulation map, it is denoted as $\bar{\psi}_{\text{S.ROI}}$. Furthermore, the Pearson correlation coefficient was computed for the Rq and the ρ_{length} , as we had enough values to ensure its relevance. The Pearson correlation coefficient measures the linear relationship between two variables, ranging from -1 to 1. It thus indicates the degree of their dependence. In the next section, we will delve into the detailed analysis of these results, exploring the relationships between the microstructural parameters and their specular responses.

4.3.2 Analysis and interpretation of the results

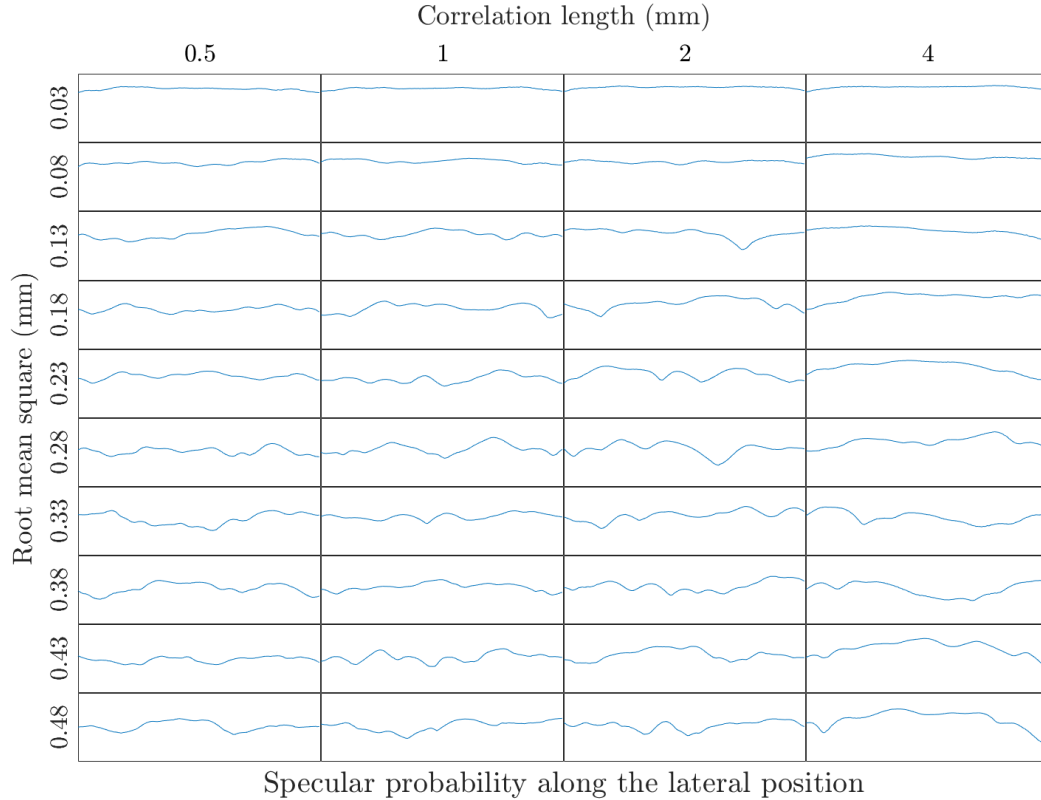


Figure 25: Mean Specularity over the lateral position $\overline{\psi_{\text{lateral}}}$. The value ranged from 0 to 1. Each case corresponds to the $\overline{\psi_{\text{lateral}}}$ of the map shown in Figure 21

Having generated the simulated surfaces, applied the specular echo method, and chosen the output metrics, we now move on to analyzing the results. The analysis of the $\overline{\psi_{\text{lateral}}}$ was performed on the simulation N°1, therefore without pores. This analysis reveals that the magnitude of the $\overline{\psi_{\text{lateral}}}$ decreases with an increasing Rq and conversely increases with a higher ρ_{length} , as shown in Figure 25. Additionally, its variation within each simulation is relatively low. The variance of the $\overline{\psi_{\text{lateral}}}$ is inferior to 3% for all the simulations, as shown in table 3. Therefore, further study of the specular response regarding the microstructure will proceed by focusing on the $\overline{\psi_{\text{S.ROI}}}$, given the low variability of the $\overline{\psi_{\text{lateral}}}$ observed within each simulation map.

For the initial simulations, we analyzed the $\overline{\psi_{\text{S.ROI}}}$ by plotting it in a 3D plane. A planar surface was then fitted to the scattered point to observe the trends in the results. As shown in Figure 26, we can confirm the observation made on the $\overline{\psi_{\text{lateral}}}$ regarding the influence of the Rq and the ρ_{length} . The observed tendency confirms our hypothesis. As previously mentioned, a higher Rq indicates greater height amplitude variations, resulting in a rougher interface and thus a lower specular index. Conversely, a higher ρ_{length} implies longer distances over which amplitude changes occur, leading to a smoother surface and consequently a higher specular index ψ .

$Rq \backslash \rho_{length}$	0.5 mm	1 mm	2 mm	4 mm
0.03 mm	0.07	0.04	0.03	0.05
0.08 mm	0.18	0.15	0.06	0.10
0.13 mm	1.00	0.44	1.07	0.45
0.18 mm	0.47	1.25	1.26	0.60
0.23 mm	0.46	0.97	1.21	1.16
0.28 mm	0.90	1.72	2.36	1.06
0.33 mm	2.65	0.57	1.58	2.16
0.38 mm	2.15	1.02	1.80	3.68
0.43 mm	0.68	1.43	1.89	2.12
0.48 mm	1.49	2.04	1.39	3.82

Table 3: Variance (%) of the $\overline{\psi}_{lateral}$, rounded to two decimal places. Each case corresponds to the results of the corresponding simulation map in Figure 21

Specifically, an increase of 0.4 mm in the Rq leads to a decrease of almost 30% in the $\overline{\psi}_{S.ROI}$, while an increase of 3 mm in the ρ_{length} results in an increase of less than 20% in the $\overline{\psi}_{S.ROI}$. The slope of the surface is steeper with respect to Rq compared to ρ_{length} . For instance, the equation of the red plan that corresponds to the simulation without pores, in Figure 26, is the following :

$$\overline{\psi}_{S.ROI} = -0.54 * Rq + 0.02 * \rho_{length} + 0.72$$

This suggests that the Rq has a greater impact on the specular response of the interface.

Pearson correlation coefficient	Mean specular index in the ROI $\overline{\psi}_{S.ROI}$
Rq [mm]	-0.7
ρ_{length} [mm]	0.3

Table 4: Pearson correlation coefficient regarding the surface parameters

The dependency of the $\overline{\psi}_{S.ROI}$ regarding the Rq is also assessed by the Pearson correlation coefficient. As shown in Table 4, the coefficient is negative between the Rq and the $\overline{\psi}_{S.ROI}$, indicating an inverse relationship, while the correlation has a positive relationship. The absolute value of the coefficient is higher for the Rq , indicating that the $\overline{\psi}_{S.ROI}$ is more related to the Rq than on the ρ_{length} .

The addition of pores also seems to influence the $\overline{\psi}_{S.ROI}$. The trend regarding the Rq and the ρ_{length} are conserved. However, the order of magnitude is greatly impacted and decreased by the presence of pores. Specifically, the addition of 7% of pores seems to reduce the $\overline{\psi}_{S.ROI}$ of 2% for equivalent values of Rq and ρ_{length} .

Due to the higher influence of the Rq , further investigation over the porosity and diameter of the pore will be performed on simulation with a single value of ρ_{length} .

The results are plotted in a 2D plan regarding the Rq . As shown in figure 27, the introduction of a 7% porosity in the one-wavelength-wide bande leads to a decrease of

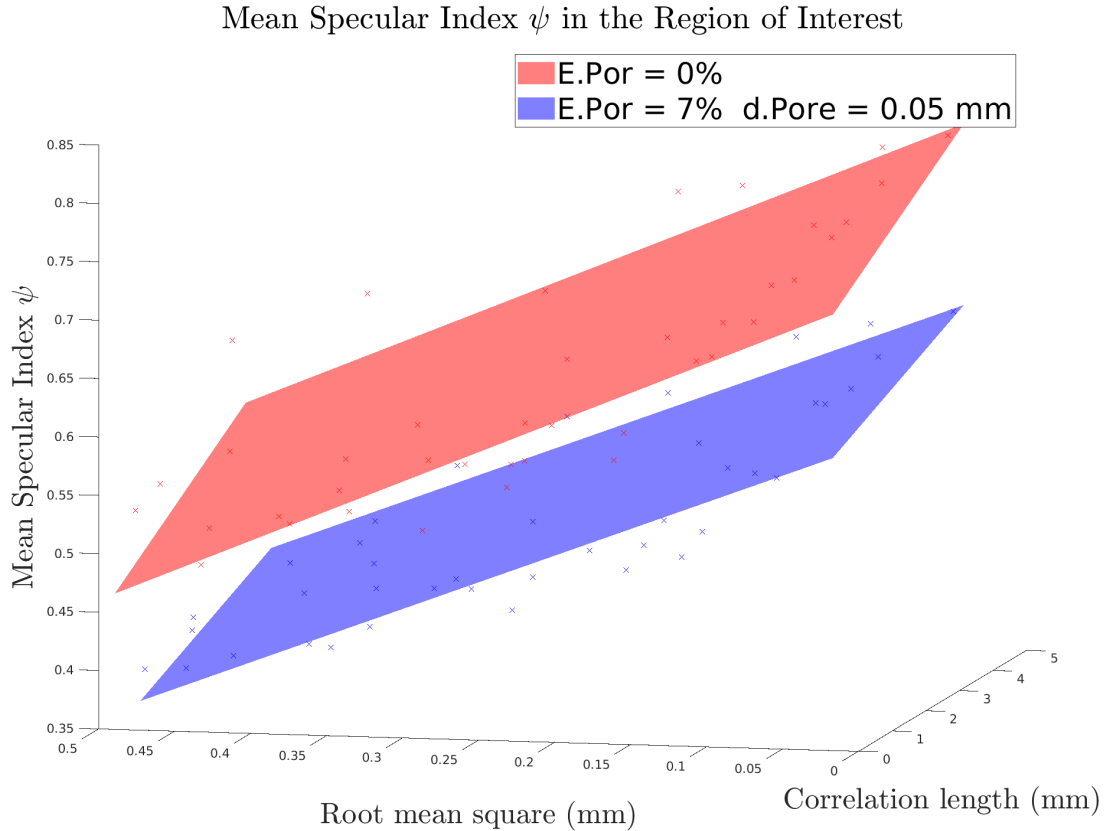


Figure 26: Mean specular index in the S.ROI, $\overline{\psi}_{S.ROI}$, regarding Rq and ρ_{length}

20% of the magnitude of the $\overline{\psi}_{S.ROI}$. When we add further porosity, up to 14%, the trend seems to change. The pore is too concentrated at the endosteal interface, its detection isn't even possible, therefore, the surface parameters aren't relevant anymore, we thus observe a low $\overline{\psi}_{S.ROI}$, around 0.1.

The study of the size of pores allows us to see that the size also influences the specular index. We observe that larger pores induce a reduction of the specularity. Pore of diameter $d.Pore = 50\mu m$ are small compared to the wavelength, so they scatter the acoustic waves in all directions. Larger pores have dimensions closer to the wavelength, causing the scattering to be less uniform [13]. This preferential scattering can interfere with the specular reflection from the interface. These larger pores thus induce more noise, leading to a decrease in the $\overline{\psi}_{S.ROI}$ of the interface.

As observed, a $\overline{\psi}_{S.ROI}$ of 0.6, for example, could correspond to a bone with either a low Rq and high porosity or pore size, or a bone with a higher Rq and lower porosity. Thus, the $\overline{\psi}_{S.ROI}$ alone does not discriminate the parameters characterizing the bone, but it provides insight into its possible microstructure. Alongside other parameters such as bone width and density, these parametric studies give information about the bone's health state. As we know high Rq and high porosity are both related to the degradation of the endosteal interface. Moreover, we considered the surface parameters (Rq and ρ_{length}) and the intra-cortical parameters ($E.Pore$ and $d.Pore$) as uncorrelated. Both of these parameters are describing the same process of degradation of the bone. It is therefore

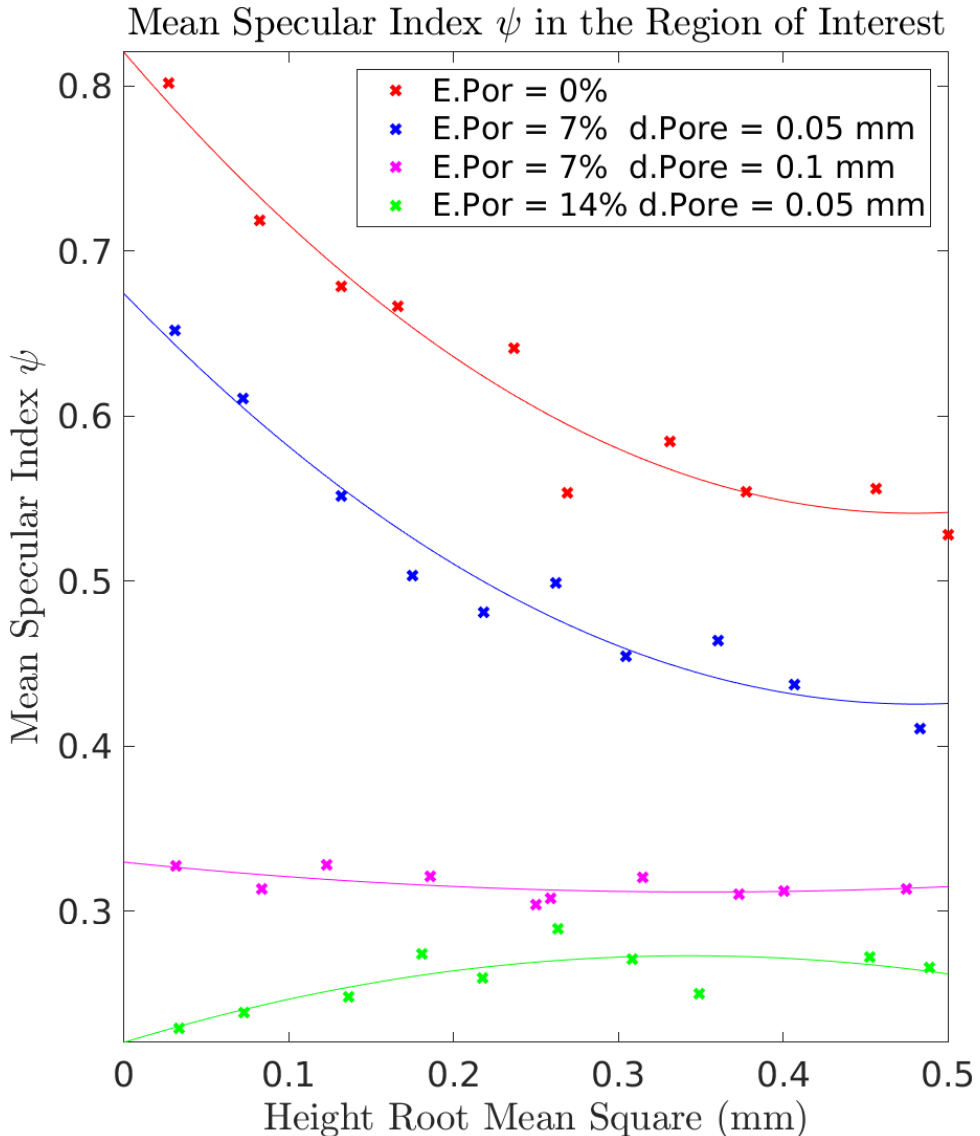


Figure 27: Mean specular index in the S.ROI, $\overline{\psi}_{S.ROI}$, regarding Rq and ρ_{length}

coherent to suppose that they are correlated. Further investigation using more realistic bone would enable us to validate our results and assess their pertinence.

5 Perspective

The study performed on the selected set of microstructures allowed us to make hypotheses about the specular response regarding the endosteal porosity and the mean pore diameter. However, the limited range of data in these simulations prevents us from making definitive conclusions. Identifying the limits of porosity and pore diameter for the detection of the endosteal interface would improve our understanding of the observed results in realistic microstructures. Improving the quantification of the degradation state in cases of very low specular index.

The study of the impact of microstructure on the specular index with generated microstructures needs to be validated by comparing them with more realistic microstructures. One approach is to use microstructures generated with a more accurate representation of bone, as previously discussed. However, due to the high computational demands of such simulations, we chose to directly simulate on maps derived from ex-vivo bone images obtained with CT scans (as shown in Figures 11a and 11b).

For the three femoral bones initially selected, we generated simulation maps for each of the four zones. The idea is to post-process these maps in the same way as the simulations on the generated profile. By doing so, we aim to validate our results against the ones obtained from the ex-vivo images.

The following step would be to compare our results with previous ex-vivo experimental measurements with an actual ultrasound probe. These measurements were performed in the LIB with the setup shown in figure 28. As shown previously, the probe is placed on an extracted part of the bone (Figure 10b). The specularity map has already been computed for these bones.

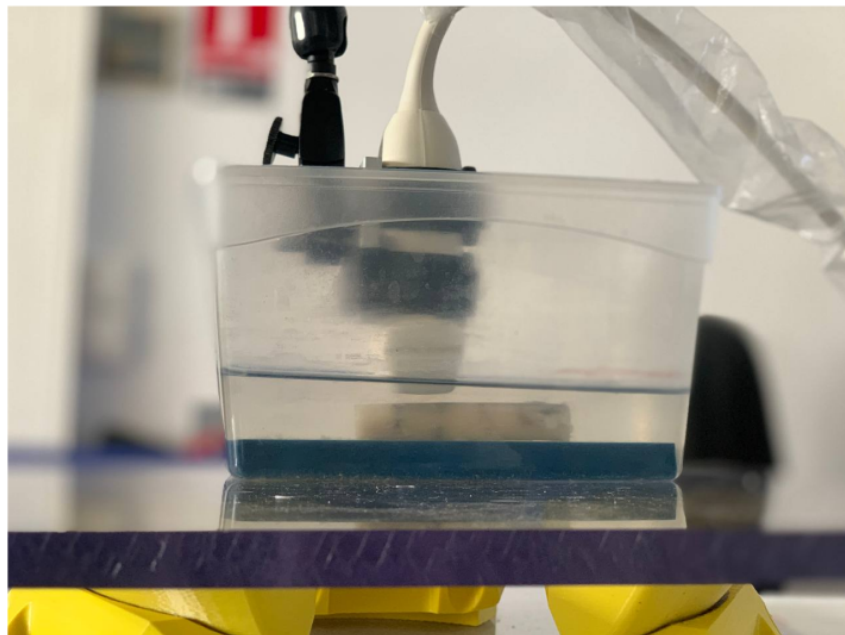


Figure 28: Experimental setup for ultrasound acquisitions, the probe positioned on the sample, submerged in water, from Dia [14]

This comparative analysis would allow us to verify the accuracy of our 2D simulation results, making sure that they are realistic and applicable for interpreting 3D ex-vivo results. This would assess that our 2D simulations are reliable and valuable for understanding bone microstructure and its effects on the specular index.

Conclusion

This study aimed to improve diagnostic methods for osteoporosis by quantifying the degradation of cortical bones to complement current diagnostic tools. Utilizing ultrasound imaging techniques developed by the Laboratory of Biomedical Imaging (LIB), we aimed to quantify the roughness of the endosteal interface, an area significantly affected by bone loss.

During this study, we described the significant impact of osteoporosis on cortical bone. We explained the ultrasound imaging methods developed by the LIB and their application to cortical bone. This adaptation of traditional soft tissue ultrasound imaging offered information about bone density and thickness.

The study was centered around determining parameters of the endosteal interface's microstructure that indicate its degradation. Using high-resolution microtomography (micro-CT) images of ex-vivo bones, we characterized both the endosteal interface and the endosteal intra-cortical region of interest (E.ROI). The parameters chosen to describe the surface are the height root mean square (Rq) and the correlation length (ρ_{length}), the E.ROI is described with a porosity parameter and the mean diameter of the pore. These parameters efficiently discriminated the bone's state of degradation. Simulations were then performed based on generated microstructures with varying values of these parameters to study their impact on acoustic response. This helped us understand how changes in the endosteal interface's microstructure affect the specular reflection of acoustic waves.

The results of these simulations enabled us to understand the responsible parameters of the specular response of the interface, concluding on the importance of the Rq of the surface, and the porosity and size of pores of the E.ROI. However, further investigation into the limits until the interface is detected regarding the intra-cortical parameters would enhance our comprehension of the cases where we cannot detect the endosteal interface.

Finally, we expressed the project's perspective, with the idea to validate these findings against more realistic microstructures derived from ex-vivo bone images, ensuring that our simulation results apply to actual bone conditions, with the larger goal of testing these techniques *in vivo*.

In summary, while this study does not yet provide a complete diagnostic solution, it advances our understanding of using ultrasound imaging to assess cortical bone roughness and degradation. The methods and findings from this research offer a foundation for future investigations, aiming to extend their application to clinical trials. This work contributes to developing more effective diagnostic tools for early detection and management of osteoporosis, potentially improving patient outcomes and quality of life.

References

- [1] Tumay Sozen, L. Ozisik, and Nursel Başaran. “An overview and management of osteoporosis”. In: *European Journal of Rheumatology* 4 (Dec. 2016). DOI: 10.5152/eurjrheum.2016.048.
- [2] URL: <https://www.lib.upmc.fr/presentation-du-laboratoire/>.
- [3] Mathilde Mouchet. “Evaluation multi-échelle de la qualité osseuse par ultrasons”. Thèse de doctorat dirigée par Laugier, Pascal Acoustique Physique Paris 7 2012. PhD thesis. 2012, 1 vol. (144 p.) URL: <http://www.theses.fr/2012PA077063>.
- [4] Judith Desoutter et al. “Le remodelage osseux normal et pathologique”. In: *Revue Francophone des Laboratoires* 2012 (Nov. 2012), 33–42. DOI: 10.1016/S1773-035X(12)71733-1.
- [5] Roger Zebaze et al. “Intracortical remodelling and porosity in the distal radius and post-mortem femurs of women: A cross-sectional study”. In: *Lancet* 375 (May 2010), pp. 1729–36. DOI: 10.1016/S0140-6736(10)60320-0.
- [6] Roger Zebaze et al. “A New Method of Segmentation of Compact-Appearing, Transitional and Trabecular Compartments and Quantification of Cortical Porosity from High Resolution Peripheral Quantitative Computed Tomographic Images.” In: *Bone* 54 (Jan. 2013). DOI: 10.1016/j.bone.2013.01.007.
- [7] Didier Hans and Sanford Baim. “Quantitative Ultrasound (QUS) in the Management of Osteoporosis and Assessment of Fracture Risk”. In: *Journal of Clinical Densitometry* 20 (July 2017). DOI: 10.1016/j.jocd.2017.06.018.
- [8] Ihor Trots et al. “Synthetic Aperture Method in Ultrasound Imaging”. In: Apr. 2011. ISBN: 978-953-307-239-5. DOI: 10.5772/15986.
- [9] Jørgen Arendt Jensen et al. “Synthetic aperture ultrasound imaging”. In: *Ultrasonics* 44 (2006). Proceedings of Ultrasonics International (UI'05) and World Congress on Ultrasonics (WCU), e5–e15. ISSN: 0041-624X. DOI: <https://doi.org/10.1016/j.ultras.2006.07.017>. URL: <https://www.sciencedirect.com/science/article/pii/S0041624X06003374>.
- [10] Vincent Perrot et al. “So you think you can DAS? A viewpoint on delay-and-sum beamforming”. In: *Ultrasonics* 111 (2021), p. 106309. ISSN: 0041-624X. DOI: <https://doi.org/10.1016/j.ultras.2020.106309>. URL: <https://www.sciencedirect.com/science/article/pii/S0041624X20302444>.
- [11] Guillaume Renaud et al. “In vivo ultrasound imaging of the bone cortex”. In: *Physics in Medicine and Biology* 63 (June 2018). DOI: 10.1088/1361-6560/aac784.
- [12] Guillaume Renaud and Salles Sébastien. “Single-Sided Ultrasound Imaging of the Bone Cortex: Anatomy, Tissue Characterization and Blood Flow”. In: vol. 1364. Nov. 2021, pp. 197–225. ISBN: 978-3-030-91978-8. DOI: 10.1007/978-3-030-91979-5_10.
- [13] Amadou Dia et al. “The influence of intra-cortical microstructure on the contrast in ultrasound images of the cortex of long bones: A 2D simulation study”. In: *Ultrasonics* 127 (Aug. 2022), p. 106831. DOI: 10.1016/j.ultras.2022.106831.

- [14] Amadou Dia. "Quantitative ultrasound imaging of human cortical bone". Thèse de doctorat dirigée par Quentin GRIMAL et Guillaume RENAUD. PhD thesis. 2024, 1 vol. (167 p.)
- [15] Alfonso Rodriguez-Molares et al. "Specular Beamforming". In: *IEEE Transactions on Ultrasonics, Ferroelectrics, and Frequency Control* 64.9 (Sept. 2017). Conference Name: IEEE Transactions on Ultrasonics, Ferroelectrics, and Frequency Control, pp. 1285–1297. ISSN: 1525-8955. DOI: 10.1109/TUFFC.2017.2709038.
- [16] Peter Ettl et al. "Roughness parameters and surface deformation measured by coherence radar". In: *Proc SPIE* 3407 (Sept. 1998), pp. 133–140. DOI: 10.1117/12.323304.
- [17] J. Raja and V. Radhakrishnan. "Digital filtering of surface profiles". In: *Wear* 57.1 (1979), pp. 147–155. ISSN: 0043-1648. DOI: [https://doi.org/10.1016/0043-1648\(79\)90148-0](https://doi.org/10.1016/0043-1648(79)90148-0). URL: <https://www.sciencedirect.com/science/article/pii/0043164879901480>.
- [18] Deden Dian Sukmana and Ikuo Ihara. "Surface Roughness Characterization through the Use of Diffuse Component of Scattered Air-Coupled Ultrasound". In: *Japanese Journal of Applied Physics* 45.5S (2006), p. 4534. DOI: 10.1143/JJAP.45.4534. URL: <https://dx.doi.org/10.1143/JJAP.45.4534>.
- [19] J.E. Wilhjelm, P.C. Pedersen, and S.M. Jacobsen. "The influence of roughness, angle, range, and transducer type on the echo signal from planar interfaces". In: *IEEE Transactions on Ultrasonics, Ferroelectrics, and Frequency Control* 48.2 (2001), pp. 511–521. DOI: 10.1109/58.911734.
- [20] Sidsel Sjøj et al. "Ultrasound pulse-echo measurements on rough surfaces with linear array transducers". In: *AIP Conference Proceedings* 1433 (May 2012), pp. 211–214. DOI: 10.1063/1.3703173.
- [21] Emmanuel Bossy, Maryline Talmant, and Pascal Laugier. "3-D simulations of ultrasonic axial transmission velocity measurement on cortical bone models". In: *The Journal of the Acoustical Society of America* 115 (June 2004), pp. 2314–24. DOI: 10.1121/1.1689960.
- [22] Gianluca David Bergström et al. "From rsgene1D.m function". In: (2017).
- [23] Gianluca Iori et al. "Estimation of Cortical Bone Microstructure From Ultrasound Backscatter". In: *IEEE Transactions on Ultrasonics Ferroelectrics and Frequency Control* PP (Oct. 2020). DOI: 10.1109/TUFFC.2020.3033050.
- [24] URL: <https://www.lib.upmc.fr/proposition-de-stage-imagerie-ultrasonore-quantitative-de-la-rugosite-application-a-levaluation-de-la-sante-osseuse/>.

A Parameters of the endosteal interface roughness on ex-vivo bones

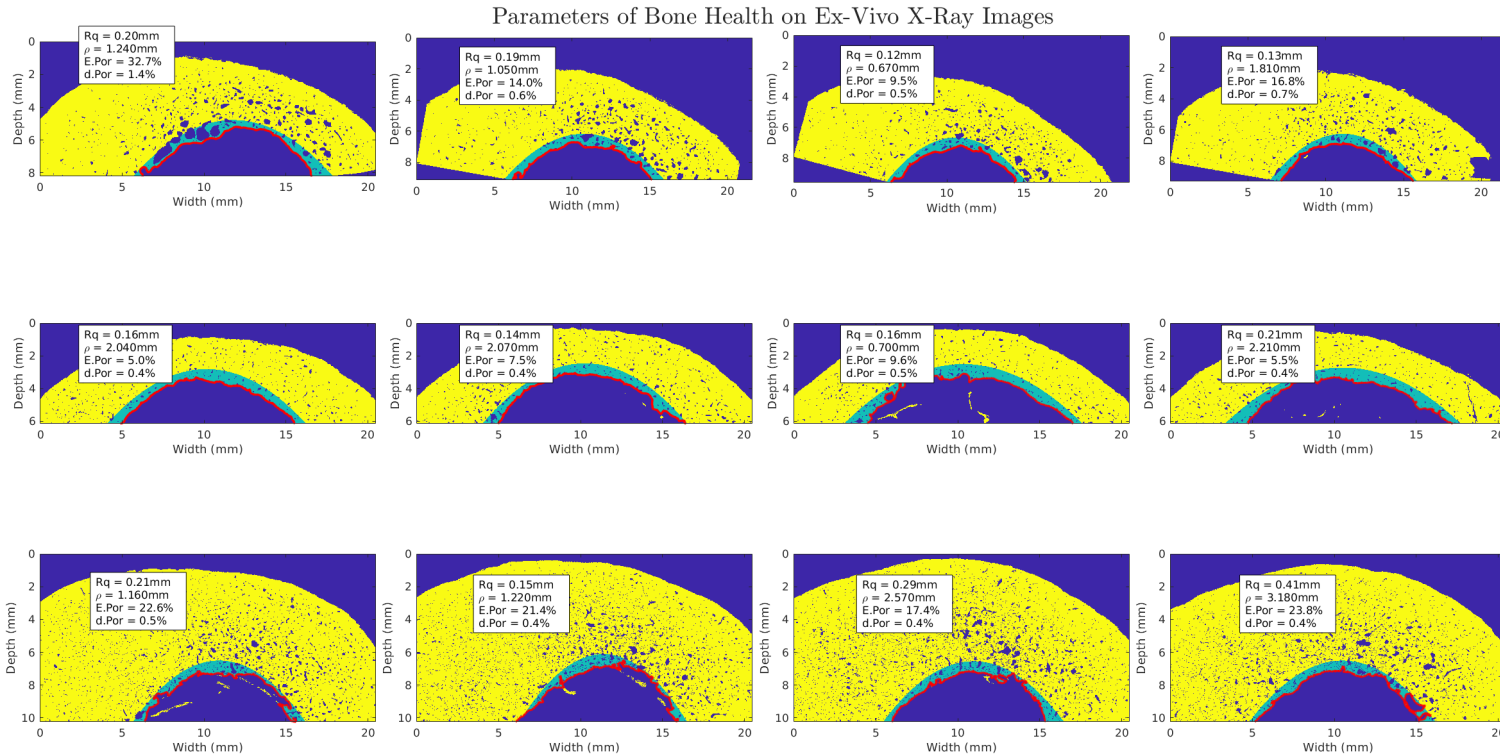
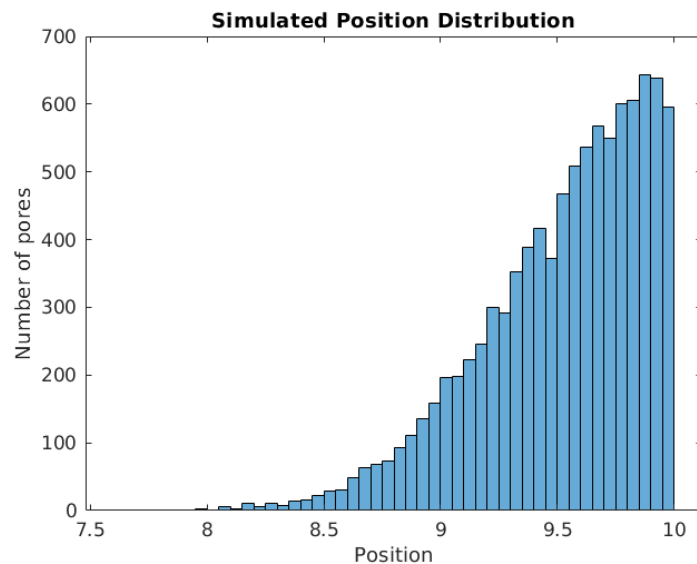


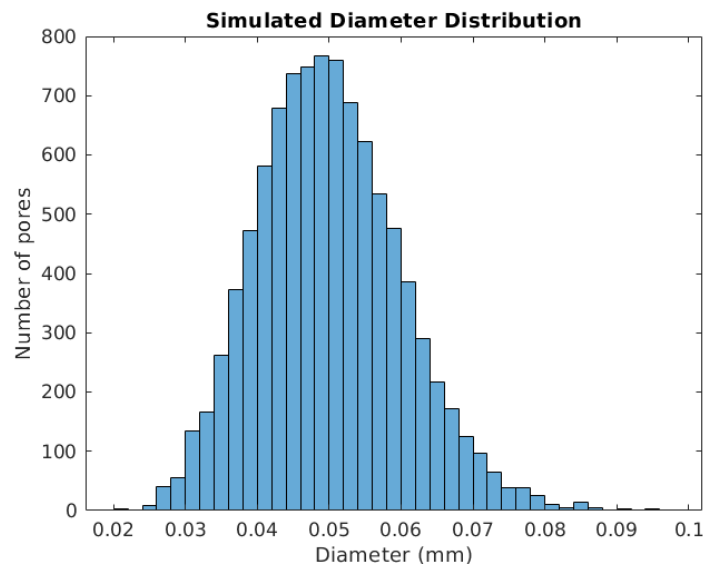
Figure 29: Parameters of the endosteal interface roughness interface for the 4 zones of interest of the three chosen femoral bones

B Histogram of the distributions of the pore position along the depth of the bone and their diameter

The distributions of the pore position along the depth of the bone (Figure 30a) and their diameter (Figure 30b) for a realistic modelization of an "aged" patient, with a porosity of 30% near the endosteal interface is shown in Figure 30.



(a) Histogram of the position of the pore along the z-axis



(b) Histogram of the diameter of the pore

Figure 30: Histogram of distributions

C Gantt diagram

The organizational diagram of my internship is shown in the following figure. The green boxes correspond to the actual plan I have followed, while the yellow boxes represent what is planned to be done after this report has been submitted.

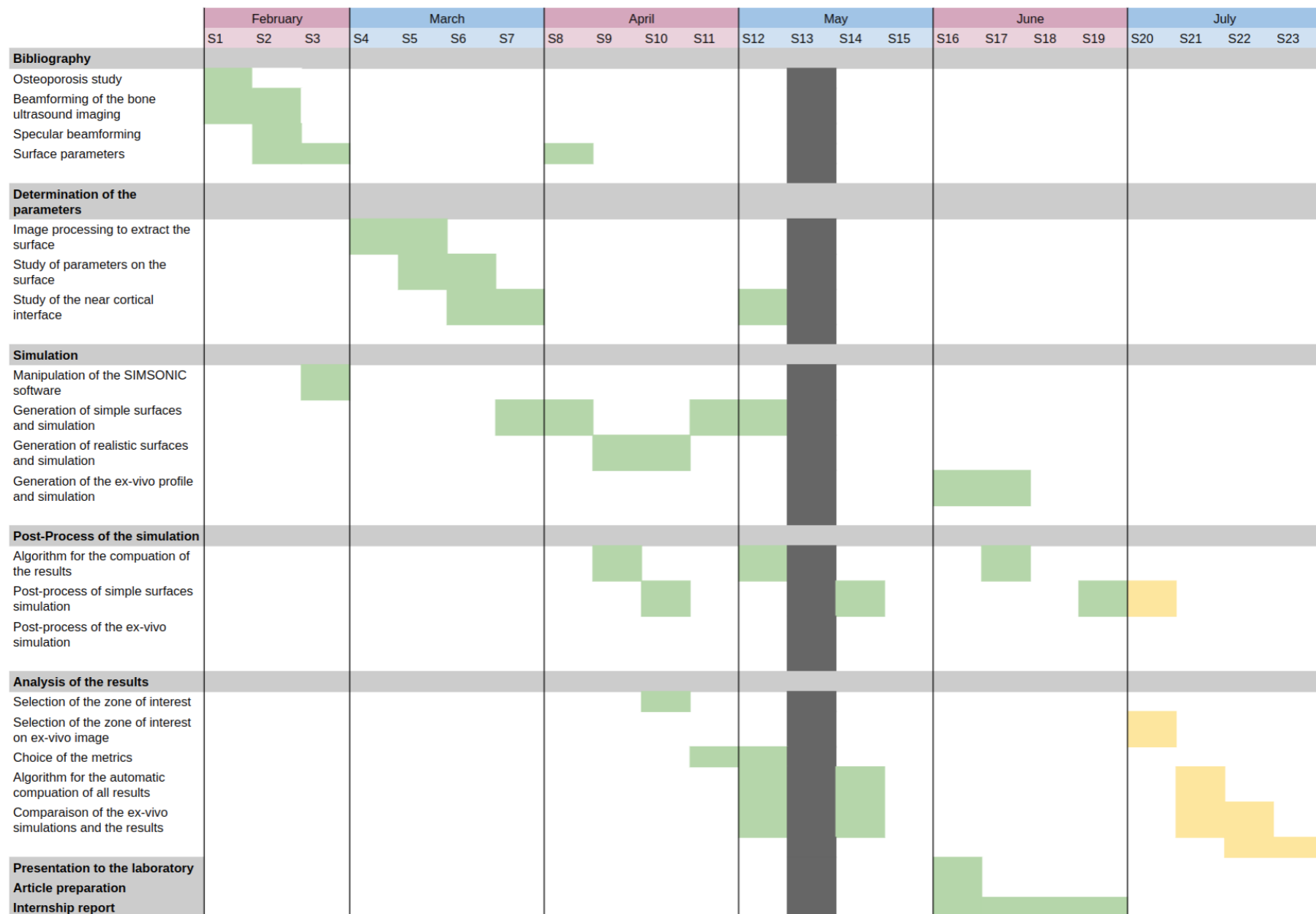


Figure 31: Gantt diagram

Abstract

Increased cortical porosity near the endosteal interface due to bone loss results in surface roughness, indicating bone degradation. Ultrasound imaging has been proposed for cortical bone surface evaluation. In this study, we quantitatively assess cortical bone rugosity using specular reflection physics. High-resolution micro-CT images of ex-vivo human bone samples were used to identify parameters characterizing the endosteal interface such as the root mean square of the height profile Rq and the correlation length (ρ_{length}). Porosity and mean pore diameter were quantified in a region of interest near the endosteal interface. Simulated profiles of the interface varied these parameters. Synthetic aperture imaging with an array transducer was simulated using a finite difference time domain elastic code, with specularity assessed via specular beamforming accounting for refraction. The mean specular index near the endosteal interface correlates more strongly with Rq than ρ_{length} . Results indicate a decrease in specular index with increasing Rq . Higher porosity and pore diameter also correlate with reduced specular index, underscoring their impact on ultrasound reflectivity and sensitivity to bone microstructure. However, distinguishing between bones with differing Rq and porosity levels remains challenging due to overlapping specular index values. Further validation through ex-vivo experiments is necessary to confirm these findings.

Résumé

Une porosité corticale accrue près de l'interface endostéale due à une perte osseuse entraîne une rugosité de surface, indiquant une dégradation osseuse. L'imagerie par ultrasons a été proposée pour l'évaluation de la surface de l'os cortical. Dans cette étude, nous évaluons quantitativement la rugosité de l'os cortical en utilisant la physique de la réflexion spéculaire. Des images micro-CT haute résolution d'échantillons d'os humains ex-vivo ont été utilisées pour identifier des paramètres caractérisant l'interface endostéale tels que la racine carrée moyenne du profil de hauteur Rq et la longueur de corrélation ρ_{length} . La porosité et le diamètre moyen des pores ont été quantifiés dans une région d'intérêt près de l'interface endostéale. Les profils simulés de l'interface variaient ces paramètres. L'imagerie par ouverture synthétique avec un transducteur en réseau a été simulée en utilisant un code élastique de type différences finies dans le domaine temporel, avec la spécularité évaluée via le beamforming spéculaire tenant compte de la réfraction. La moyenne de l'indice spéculaire près de l'interface endostéale corrèle plus fortement avec Rq qu'avec ρ_{length} . Les résultats indiquent une diminution de l'indice spéculaire avec l'augmentation de Rq . Une porosité et un diamètre moyen des pores plus élevés corrèlent également avec une réduction de l'indice spéculaire, soulignant leur impact sur la réflectivité des ultrasons et la sensibilité à la microstructure osseuse. Cependant, distinguer entre des os avec des niveaux différents de Rq et de porosité reste difficile en raison de la superposition des valeurs de l'indice spéculaire. Une validation supplémentaire par des expériences ex-vivo est nécessaire pour confirmer ces résultats.

Fiche résumé

Salomé Vignat

Filière Biomédicale, option imagerie médical et thérapie (MEDIT) Année universitaire 2023/2024

Titre du stage

Imagerie ultrasonore quantitative de la rugosité, application à l'évaluation de la santé osseuse.

Période du stage: 12 février au 02 août.

Laboratoire

Laboratoire d'Imagerie Biomédical
15 rue de la Médecine 75006 Paris



Responsable de stage

Quentin Grimal

quentin.grimal@sorbonne-universite.fr

Tuteur école

Charlotte Vendrelly

charlotte.Vendrelly@grenoble-inp.fr

Descriptif du stage

Contexte

Les tissus du corps humain sont des milieux visco-élastiques et hétérogènes. Les principes physiques de la propagation des ondes dans ces milieux sont exploités pour reconstruire des images à partir de signaux recueillis par une sonde d'échographie. Les images sont quantitatives lorsqu'elles reflètent autre chose que les frontières anatomiques des organes : l'élasticité, la composition chimique, la taille caractéristiques des cellules, etc. Dans certaines pathologies du tissus osseux, comme l'ostéoporose, la face interne de l'os cortical devient « rugueuse » suite à une action désordonnée des cellules impliquées dans le remodelage osseux. Une surface rugueuse donne lieu à une réflexion beaucoup plus diffuse des ultrasons qu'une surface lisse qui donne essentiellement lieu à une réflexion spéculaire selon les lois de la réflexion de Descartes. L'ostéoporose est une pathologie du remodelage osseux dont le diagnostique est un enjeux de santé publique. Le coût du traitement des fractures associés est de l'ordre de celui du traitement de l'infarctus du myocarde ou du cancer du sein. L'ostéoporose est actuellement insuffisamment détectée de sorte que

de nombreux patients ne peuvent pas bénéficier des traitements existants. A terme, la mesure de la rugosité des interfaces osseuses avec un appareil d'échographie permettrait d'évaluer l'activité de remodelage osseux chez les patients de manière non invasive, et donc leur santé osseuse.

Objectif

Au LIB, nous développons une méthode qui permet de séparer les contributions des réflexions diffuses vs. spéculaires à une interface. L'objectif du stage est de poursuivre le développement de cette méthode pour réaliser une imagerie quantitative des interfaces osseuses, c'est-à-dire de cartographier la rugosité. Il s'agira, entre autres choses, de proposer une méthode de calibrage permettant de remonter aux valeurs « vraies » de la rugosité à partir du signal ultrasonore. Le stagiaire utilisera un échographe programmable pour faire des expériences sur différents objets de rugosité contrôlée. Il ou elle utilisera également la simulation pour comprendre les mécanismes de la formation des images. Enfin des signaux obtenus sur des échantillons d'os ex vivo et chez des sujets (in vivo) seront exploités pour évaluer le potentiel clinique de la méthode. [24]

Moyens et encadrement

Durant ce stage, j'ai disposé d'un bureau individuel et d'un ordinateur fixe possédant une grande capacité de stockage. J'ai disposé du logiciel Matlab © ainsi que du logiciel SimSonic ©. En plus du responsable de stage j'ai grandement travaillé avec Amadou S. Dia, doctorant travaillant sur l'imagerie ultrasonore quantitative de l'os cortical humain.